The Astrophysical Journal, 971:141 (20pp), 2024 August 20 https://doi.org/10.3847/1538-4357/ad4d55

# Circumstellar Interaction Signatures in the Low-luminosity Type II SN 2021gmj

Nicolás Meza-Retamal[1], Yize Dong (董一泽)[1], K. Azalee Bostroem[2,19], Stefano Valenti[1], Lluís Galbany[3,4], Jeniveve Pearson[2], Griffin Hosseinzadeh[2], Jennifer E. Andrews[5], David J. Sand[2], Jacob E. Jencson[2], Daryl Janzen[6], Michael J. Lundquist[7], Emily T. Hoang[1], Samuel Wyatt[8], Peter J. Brown[9], D. Andrew Howell[10,11], Megan Newsome[10,11], Estefania Padilla Gonzalez[10,11], Craig Pellegrino[10,11], Giacomo Terreran[10,11], Vladimir Kouprianov[12], Daichi Hiramatsu[13,14], Saurabh W. Jha[15], Nathan Smith[2], Joshua Haislip[12], Daniel E. Reichart[12], Manisha Shrestha[2], F. Fabián Rosales-Ortega[16], Thomas G. Brink[17], Alexei V. Filippenko[17], WeiKang Zheng[17], and Yi Yang[17,18]

[1] Department of Physics and Astronomy, University of California Davis, 1 Shields Avenue, Davis, CA 95616-5270, USA; nemezare@ucdavis.edu
[2] Steward Observatory, University of Arizona, 933 North Cherry Avenue, Tucson, AZ 85721-0065, USA
[3] Institute of Space Sciences (ICE, CSIC), Campus UAB, Carrer de Can Magrans, s/n, E-08193 Barcelona, Spain
[4] Institut d'Estudis Espacials de Catalunya, Gran Capità, 2-4, Edifici Nexus, Desp. 201, E-08034 Barcelona, Spain
[5] Gemini Observatory, 670 North A'ohoku Place, Hilo, HI 96720-2700, USA
[6] Department of Physics & Engineering Physics, University of Saskatchewan, 116 Science Place, Saskatoon, SK S7N 5E2, Canada
[7] W.M. Keck Observatory, 65-1120 Māmalahoa Highway, Kamuela, HI 96743-8431, USA
[8] Department of Astronomy, University of Washington, 3910 15th Avenue NE, Seattle, WA 98195-0002, USA
[9] Department of Physics and Astronomy, Texas A&M University, 4242 TAMU, College Station, TX 77843, USA
[10] Las Cumbres Observatory, 6740 Cortona Drive, Suite 102, Goleta, CA 93117-5575, USA
[11] Department of Physics, University of California, Santa Barbara, CA 93106-9530, USA
[12] Department of Physics and Astronomy, University of North Carolina, 120 East Cameron Avenue, Chapel Hill, NC 27599, USA
[13] Center for Astrophysics | Harvard & Smithsonian, 60 Garden Street, Cambridge, MA 02138-1516, USA
[14] The NSF AI Institute for Artificial Intelligence and Fundamental Interactions, USA
[15] Department of Physics and Astronomy, Rutgers, the State University of New Jersey, 136 Frelinghuysen Road, Piscataway, NJ 08854-8019, USA
[16] Instituto Nacional de Astrofísica, Óptica y Electrónica (INAOE CONACyT), Luis E. Erro 1, 72840, Tonantzintla, Puebla, Mexico
[17] Department of Astronomy, University of California, Berkeley, CA 94720-3411, USA
[18] Physics Department and Tsinghua Center for Astrophysics, Tsinghua University, Beijing 100084, People's Republic of China

*Received 2024 January 15; revised 2024 May 10; accepted 2024 May 11; published 2024 August 13*

## Abstract

We present comprehensive optical observations of SN 2021gmj, a Type II supernova (SN II) discovered within a day of explosion by the Distance Less Than 40 Mpc survey. Follow-up observations show that SN 2021gmj is a low-luminosity SN II (LL SN II), with a peak magnitude $M_V = -15.45$ and an Fe II velocity of ∼1800 km $s^{-1}$ at 50 days past explosion. Using the expanding photosphere method, we derive a distance of $17.8^{+0.6}_{-0.4}$ Mpc. From the tail of the light curve we obtain a radioactive nickel mass of $M_{^{56}\mathrm{Ni}} = 0.014 \pm 0.001\ M_\odot$. The presence of circumstellar material (CSM) is suggested by the early-time light curve, early spectra, and high-velocity Hα in absorption. Analytical shock-cooling models of the light curve cannot reproduce the fast rise, supporting the idea that the early-time emission is partially powered by the interaction of the SN ejecta and CSM. The inferred low CSM mass of 0.025 $M_\odot$ in our hydrodynamic-modeling light-curve analysis is also consistent with our spectroscopy. We observe a broad feature near 4600 Å, which may be high-ionization lines of C, N, or/and He II. This feature is reproduced by radiation-hydrodynamic simulations of red supergiants with extended atmospheres. Several LL SNe II show similar spectral features, implying that high-density material around the progenitor may be common among them.

*Unified Astronomy Thesaurus concepts:* Core-collapse supernovae (304); Type II supernovae (1731); Circumstellar matter (241); Stellar mass loss (1613); Red supergiant stars (1375)

## 1. Introduction

Core-collapse supernovae (CCSNe) result from the explosion of massive stars (>8 $M_\odot$). When a massive star retains more than $\gtrsim$1–2 $M_\odot$ of its hydrogen envelope, it explodes as a Type II supernova (SN II; see Woosley et al. 1994; Sravan et al. 2019; Hiramatsu et al. 2021a; Gilkis & Arcavi 2022). Recent studies have found the photometric and spectral properties of SNe II to be diverse (Anderson et al. 2014a; Sanders et al. 2015; Galbany et al. 2016; Rubin et al. 2016; Valenti et al. 2016; de Jaeger et al. 2019; Pessi et al. 2019; Hiramatsu et al. 2021a). SNe II exhibit a large range of peak luminosities, from −14 to −19 mag in the $V$ band (Anderson et al. 2014a; Valenti et al. 2016). After the initial rise in luminosity, the onset of hydrogen recombination triggers the plateau phase where the luminosity is roughly constant. During the plateau phase they also show a wide range of photometric decline rates that may correlate with the amount of hydrogen retained by the progenitor preexplosion (e.g., Popov 1993; Anderson et al. 2014a; Faran et al. 2014; Gutiérrez et al. 2014; Moriya et al. 2016; Hillier & Dessart 2019). In addition, the light-curve properties of SNe II show heterogeneity at early phases (e.g., rise times, peak brightness, and initial decline rates) that has been attributed to the interaction of the ejecta with circumstellar material (CSM; Morozova et al. 2017, 2018; Hosseinzadeh et al. 2023; Subrayan et al. 2023).

---

[19] LSSTC Catalyst Fellow.

Since the discovery of SN 1997D (de Mello et al. 1997; Turatto et al. 1998), SNe II that are particularly faint have been labeled low-luminosity SNe II (LL SNe II). LL SNe II have a peak $M_V > -16$ mag (Spiro et al. 2014; Müller-Bravo et al. 2020), along with narrow spectral features (indicating low expansion velocities; Pastorello et al. 2004; Spiro et al. 2014), suggesting explosion energies less than 1 foe.[20] In addition, LL SNe II decline more slowly during both the plateau and radioactive-decay light-curve phases than other Type IIP SNe (Anderson et al. 2014a; Valenti et al. 2016).

There are two scenarios that explain their observational characteristics. The first results from the explosion of a high-mass star, $\sim 25\ M_\odot$, where material remains bound to the core postcollapse, forming a black hole as a remnant. In this scenario the total ejected mass is high, $\sim 20\ M_\odot$, but the radioactive yield is severely reduced owing to fallback onto the remnant (Zampieri et al. 1998). Second, Chugai & Utrobin (2000) proposed a scenario where the progenitor is a low-mass 8–12 $M_\odot$ zero-age main-sequence (ZAMS) star. Under this assumption the ejecta mass is lower, $\sim$6–9 $M_\odot$, and the radioactive material is meager owing to the low mass of the progenitor's iron core. Progenitor studies of SNe II using direct imaging have found SNe II progenitors to be red supergiants (RSGs) with ZAMS masses $\lessapprox 20\ M_\odot$ (Smartt 2009, 2015). Similar results have been obtained through hydrodynamical models (Dessart et al. 2013; Spiro et al. 2014; Martinez & Bersten 2019). The lack of observations of high-mass progenitors favors the aforementioned low-mass progenitor scenario for LL SNe II (Spiro et al. 2014). However, this conclusion may be biased by the fact that massive progenitors are intrinsically more rare and that LL SNe II are more difficult to discover.

The early-time spectra of SNe II, within a few days after explosion, may also give us insight into the progenitors. In some instances, early spectra show narrow emission features which quickly disappear within days. The most common interpretation of these "flash features" is that they are produced by recombination of CSM after being ionized by the "flash" of hard radiation coming from either the shock breakout or CSM–ejecta interaction (e.g., Niemela et al. 1985; Garnavich & Ann 1994; Leonard et al. 2000; Matheson et al. 2000; Quimby et al. 2007; Gal-Yam et al. 2014; Shivvers et al. 2015; Yaron et al. 2017; Hosseinzadeh et al. 2018; Hiramatsu et al. 2021b; Bruch et al. 2021; Tartaglia et al. 2021). These features have recently been observed to occur in $\sim$30% of SNe II (Bruch et al. 2021). Khazov et al. (2016) suggest that the presence of flash features is related to SN luminosity, with the SNe in their sample only showing flash features for peak magnitudes $M_R < -17.5$ mag; consistent with this, the Bruch et al. (2021) sample found that SNe without flash features are on average fainter. Despite that, recent studies have found LL SNe II with early spectral features related to CSM: SN 2016bkv (Hosseinzadeh et al. 2018), which was an LL SN II with flash features, and SN 2018lab (Pearson et al. 2023), which showed a broad emission ledge feature near 4600 Å that was attributed to CSM interaction. Further study on the frequency of spectral features related to CSM in LL SNe II is required to understand the role of CSM in the diverse range of progenitors of SNe II.

In this paper, we present optical observations and an analysis of SN 2021gmj, an LL SN II that shows early signatures indicative of CSM. Section 2 outlines the observations and data-reduction procedures. The reddening along the line of sight toward SN 2021gmj is estimated in Section 3. Section 4 describes the properties of NGC 3310, the host galaxy of SN 2021gmj. In Section 5, we estimate the distance to SN 2021gmj with the expanding photosphere method (EPM). Section 6 goes on to describe the photometric evolution, including a multiband and pseudobolometric comparison with other LL SNe II. We obtain the radioactive nickel mass in Section 7. Following this measurement, in Section 8 we study the early-time light curve with analytic and hydrodynamic models to constrain the progenitor properties. Section 9 characterizes the spectroscopic observations of SN 2021gmj and describes the overall evolution, together with the early spectral features and possible signatures of CSM interaction. We then derive the (low) progenitor mass of SN 2021gmj through an analysis of nebular spectra in Section 10. In Section 11, we discuss the analysis performed and its implications. Our conclusions are presented in Section 12.

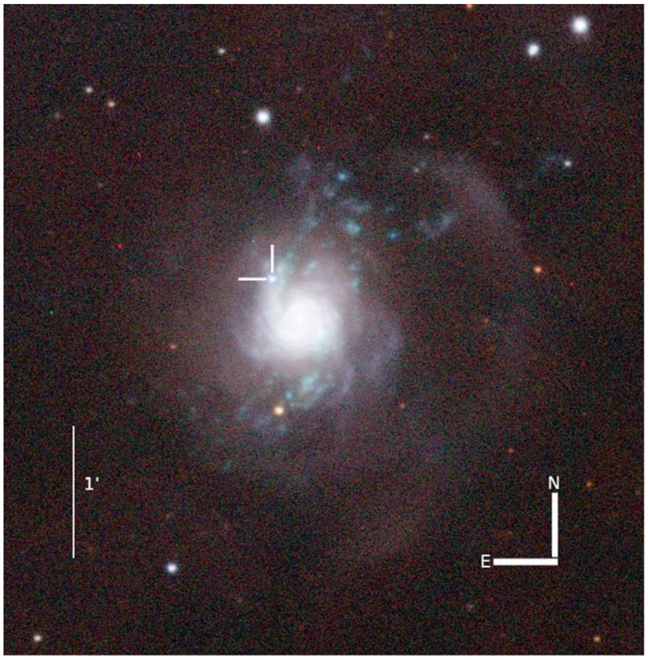

**Figure 1.** Red, green, blue image of SN 2021gmj, marked by white ticks to the northeast of the core of the galaxy NGC 3310, using *gri* images obtained with the Las Cumbres Observatory (LCO). The images were taken on 2021 March 20, one day after the estimated explosion of SN 2021gmj.

## 2. Observations and Data Reduction

SN 2021gmj was discovered at R.A. (J2000) = $10^{\mathrm{h}}38^{\mathrm{m}}47\overset{\mathrm{s}}{.}17$, decl. (J2000) = $+53°30'31''.0$ in the galaxy NGC 3310 (Figure 1) with the PROMPT-USASK telescope at Sleaford Observatory, Canada on 2021 March 20.32 (UTC dates are used throughout this paper; JD 2459293.82) at an apparent $r$ magnitude of 15.98 mag (Valenti et al. 2021) as part of the Distance Less Than 40 Mpc Survey (DLT40; Tartaglia et al. 2018). A nondetection $\sim$24 hr earlier (JD 2459292.82), with a limiting magnitude of $r \geqslant 19.1$ mag, constrains the explosion epoch. The SN was independently detected by the Zwicky Transient Facility (ZTF; Bellm et al. 2019; Graham et al. 2019) on the same night as the reported discovery in the $g$ and $r$ bands at 16.0 mag and 16.3 mag, respectively, at JD 2459293.74 or 2021 March 20.24 (Zimmerman et al. 2021). Given the

---

[20] 1 foe = $10^{51}$ erg.

**Table 1**
Basic Properties of SN 2021gmj Used Here

| Property | Value |
|---|---|
| R.A. (J2000) | $10^{\mathrm{h}}38^{\mathrm{m}}47^{\mathrm{s}}.17$ |
| Decl. (J2000) | $+53°30'31''.0$ |
| Last nondetection | JD 2459292.82 |
| First detection | JD 2459293.74 |
| Explosion epoch | JD 2459293.3 ± 0.5 |
| Host | NGC 3310 |
| Host Redshift | 0.00331 |
| $E(B-V)_{\mathrm{MW}}$ | $0.0192 \pm 0.0005$ mag |
| $E(B-V)_{\mathrm{host}}$ | $0.03 \pm 0.01$ mag |
| Distance | $17.8^{+0.6}_{-0.4}$ Mpc |
| $V_{\max}$ | $-15.46 \pm 0.08$ mag |
| $s_2(V)$ | $0.004 \pm 0.001$ mag (50 days)$^{-1}$ |

well-constrained last nondetection from the DLT40 observations, we adopt an explosion date of 2021 March 19.78 throughout this paper. This date corresponds to the midpoint between the last nondetection and the discovery. The explosion epoch and error is then $t_0 = \mathrm{JD}\ 2459293.28 \pm 0.46$. In Table 1 we show basic information and parameters of SN 2021gmj derived in this work.

Shortly after discovery, high-cadence observations were triggered with the LCO (Brown et al. 2013) and with the Neil Gehrels Swift Observatory (Gehrels et al. 2004). Las Cumbres photometric data were reduced using the PyRAF-based pipeline LCOGTSNPIPE (Valenti et al. 2016). Apparent magnitudes were calibrated using the Sloan ($g$, $r$, $i$) and APASS ($B$, $V$) catalogs. Owing to the high background emission from the host at or near the SN location, photometry was obtained after template subtraction using HOTPANTS (Becker 2015). The templates used were obtained through the same instruments: Sinistro for the 1 m data (Brown et al. 2011) and MuSCAT3 (Narita et al. 2020) for the single 2 m epoch. Swift UVOT images were reduced as described by Brown et al. (2009). The SN coincidence-loss-corrected counts were obtained with a 5″ aperture radius. The galaxy background coincidence-loss-corrected counts were extracted from the same region using a template image obtained in 2021 October. We use updated zero-points that supersede those of Breeveld et al. (2011) to obtain the final calibrated magnitudes, with time-dependent sensitivity corrections updated in 2020.[21] Unfiltered (*Open*) DLT40 images were processed with a PyRAF-based pipeline. Background contamination was removed by subtracting a reference image, and the aperture photometry was extracted from the subtracted images. The final photometry is calibrated to the $r$ band using the APASS catalog. Light curves are shown in Figure 2.

Spectroscopic observations of SN 2021gmj started on 2021 March 20, ∼1 day after discovery. The first spectrum was taken with the Liverpool Telescope (LT), which showed SN 2021gmj to be a young SN II (Perley 2021). Another early spectrum was taken with the Ekar Copernico Telescope on 2021 March 21, confirming the classification of SN 2021gmj as an SN II (Ciroi et al. 2021). Our follow-up spectroscopy started on 2021 March 21 with Binospec (Fabricant et al. 2019) on the 6.5 m MMT telescope and the FLOYDS spectrograph (Brown et al. 2013) on the 2 m Faulkes Telescope North. We also obtained spectra with the Kast spectrograph on the 3 m Shane telescope at Lick Observatory, as well as with LRIS and DEIMOS on the Keck 10 m telescopes.

The FLOYDS spectra were reduced following standard procedures using the FLOYDS pipeline (Valenti et al. 2014). The MMT data were triggered using PyMMT (Shrestha et al. 2024) and reduced using the Binospec pipeline (Kansky et al. 2019). Kast spectra were reduced using standard IRAF/Pyraf (Science Software Branch at STScI 2012) and Python routines for bias/overscan subtractions and flat-fielding. Finally, the LRIS and DEIMOS data were reduced using standard methods with the PypeIt data-reduction pipeline (Prochaska et al. 2020). A summary of spectroscopic observations is given in Table 2.

## 3. Reddening

For the Milky Way line-of-sight reddening of SN 2021gmj we use the dust map from Schlafly & Finkbeiner (2011); it gives $E(B-V)_{\mathrm{MW}} = 0.0192 \pm 0.0005$ mag. The medium-resolution MMT spectra taken on 2021 April 1 and 2021 April 17 show Na I D lines from the Milky Way and NGC 3310. Host Na I D lines, λ5890 (D2) and λ5896 (D1), in both medium-resolution spectra were measured, giving equivalent width (EW) values of 0.08 Å and 0.19 Å on 2021 April 1 and 0.07 Å and 0.14 Å on 2021 April 17 for D1 and D2, respectively. Both epoch measurements are consistent within ∼25% of each other. Using Equation (9) from Poznanski et al. (2012), we find $E(B-V)_{\mathrm{host}} = 0.03 \pm 0.01$ mag. Another method for estimating the reddening uses the diffuse interstellar band absorption at 5780 Å. However, this feature is not seen in any spectrum of SN 2021gmj, consistent with the low reddening derived from the Na I D lines (Phillips et al. 2013).

As a sanity check of our estimated reddening, we compared SN 2021gmj's colors to those of other SNe II. The color evolution of SNe II correlates with the slope of the $V$-band light curve (de Jaeger et al. 2018). For this reason we compare the $B-V$ color curve of SN 2021gmj to that of LL SNe II with similar $V$-band slope. To select the sample we used the Davis SN database[22] and retrieved the measured $V$-band slope of the plateau ($s_{50}$) and the $V$-band maximum ($V_{\max}$). In this 2D parameter space of ($s_{50}$, $V_{\max}$) we want to select the SNe that are similar to SN 2021gmj. We calculated a "distance" taking into account the variance in each parameter. This distance, called the Mahalanobis distance (Bartkowiak & Jakimiec 1989; De Maesschalck et al. 2000; Masnan et al. 2015), between two vectors $\boldsymbol{x}$ (in this case $\boldsymbol{x}$ represents the $s_{50}$–$V_{\max}$ duple for SN 2021gmj) and $\boldsymbol{y}$ (vector for the comparison SN) is evaluated as

$$d(x, y) = \sum_{i \in 1,2} \frac{(x_i - y_i)^2}{\sigma_{x_i}^2}, \tag{1}$$

where $\sigma_{x_i}^2$ is the standard deviation for the corresponding parameter. After measuring the distances between SN 2021gmj and all the SNe we selected the 16 nearest SNe. In Figure 3 we show a $s_{50}$ versus $V_{\max}$ scatterplot with SN 2021gmj and the comparison sample highlighted. In Table 3, the sample properties are listed. Out of this list of 16 we picked the closest 10 that had the required data to compare the $B-V$ color. Additionally, we included SN 2006bp as it is an object that shows spectral features similar to those of SN 2021gmj (see Section 9.5). The resulting color curves can be seen in

---

[21] https://heasarc.gsfc.nasa.gov/FTP/caldb/data/swift/uvota/

[22] http://dark.physics.ucdavis.edu/sndavis/transient

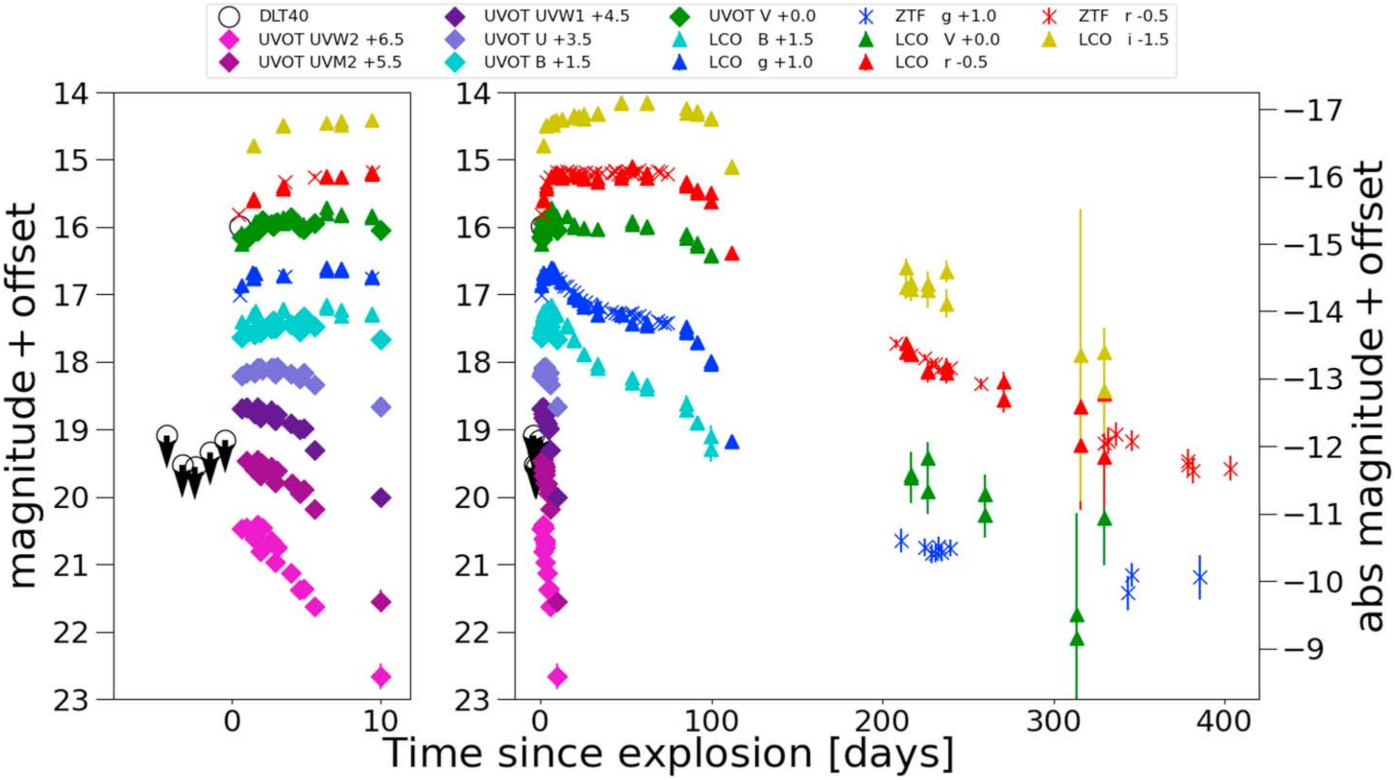

**Figure 2.** Optical and UV light curves of SN 2021gmj. The left panel contains a zoom-in of the first 10 days of observations, while the right panel shows the full light curves of Las Cumbres *BVgri* photometry with the addition of ZTF, UVOT, and DLT40 detections and nondetections. All the photometry was obtained from difference imaging, which was essential owing to significant host contamination. Preexplosion nondetections from the DLT40 survey are shown with downward-pointing arrows.

**Table 2**
Log of Optical Spectroscopic Observations

| UTC Date | MJD | Phase (days) | Wavelength range (Å) | Telescope/Instrument |
|---|---|---|---|---|
| 2021-03-20 | 59293.86 | 1.08 | 4020–7994 | LT/SPRAT |
| 2021-03-21 | 59294.06 | 1.28 | 3383–8174 | EKAR/AFOSC |
| 2021-03-21 | 59294.11 | 1.33 | 3827–9198 | MMT/Binospec |
| 2021-03-22 | 59295.23 | 2.45 | 3200–10000 | LCO-2 m/FLOYDS |
| 2021-03-23 | 59296.15 | 3.37 | 3827–9198 | MMT/Binospec |
| 2021-03-26 | 59299.47 | 6.69 | 3200–10000 | LCO-2 m/FLOYDS |
| 2021-03-28 | 59301.23 | 8.45 | 3200–10000 | LCO-2 m/FLOYDS |
| 2021-04-01 | 59305.13 | 12.35 | 5688–7210 | MMT/Binospec |
| 2021-04-02 | 59306.32 | 13.54 | 3200–10000 | LCO-2 m/FLOYDS |
| 2021-04-05 | 59309.16 | 16.38 | 3620–10720 | Shane/Kast |
| 2021-04-08 | 59312.4 | 19.62 | 3200–10000 | LCO-2 m/FLOYDS |
| 2021-04-14 | 59318.28 | 25.5 | 3622–10750 | Shane/Kast |
| 2021-04-14 | 59318.42 | 25.64 | 3200–10000 | LCO-2 m/FLOYDS |
| 2021-04-17 | 59321.21 | 28.43 | 5688–7210 | MMT/Binospec |
| 2021-04-18 | 59322.18 | 29.4 | 3632–10680 | Shane/Kast |
| 2021-04-22 | 59326.32 | 33.54 | 3200–10000 | LCO-2 m/FLOYDS |
| 2021-04-28 | 59332.32 | 39.54 | 3200–10000 | LCO-2 m/FLOYDS |
| 2021-05-09 | 59343.32 | 50.54 | 3642–10690 | Shane/Kast |
| 2021-05-15 | 59349.16 | 56.38 | 5207–7703 | MMT/Binospec |
| 2021-05-18 | 59352.28 | 59.5 | 3628–10752 | SHANE/KAST |
| 2021-05-28 | 59362.3 | 69.52 | 3200–10000 | LCO-2 m/FLOYDS |
| 2021-06-05 | 59370.31 | 77.53 | 3626–10754 | Shane/Kast |
| 2021-06-14 | 59296.15 | 86.42 | 3622–10750 | Shane/Kast |
| 2021-10-11 | 59496.61 | 203.83 | 4401–9126 | DEIMOS/Keck |
| 2021-11-03 | 59521.5 | 228.72 | 3624–10,720 | Shane/Kast |
| 2022-01-31 | 59349.16 | 317.26 | 3154–10276 | LRIS/Keck |
| 2022-06-21 | 59695.34 | 402.56 | 5380–10311 | LRIS/Keck |

**Note.** The phase is relative to our estimated explosion epoch $t_0 = \text{JD } 2459293.28 \pm 0.46$.

**Table 3**
Sample of Low-luminosity Type II Supernovae

| Name | Explosion Date (JD) | $z$ | $\mu$ (mag) | $E(B-V)_{\rm MW}$ (mag) | $E(B-V)_{\rm host}$ (mag) | $s_2(V)$ | $V_{\rm max}$ (mag) | Reference(s) |
|---|---|---|---|---|---|---|---|---|
| 1992ba | 2448889.00 ± 8.00 | 0.00411 | 31.07 ± 0.30 | 0.05 | 0.02 | 0.36 ± 0.02 | −16.05 ± 0.40 | 1, 9, 12, 16 |
| 1999bg | 2451251.50 ± 14.00 | ⋯ | 31.83 ± 0.32 | 0.02 | 0.00 | 0.32 ± 0.04 | −16.15 ± 0.32 | 10 |
| 2002gd | 2452552.00 ± 2.00 | 0.00895 | 32.90 ± 0.21 | 0.06 | 0.00 | 0.35 ± 0.05 | −15.89 ± 0.21 | 9, 10, 12, 16, 17 |
| 2002gw | 2452560.00 ± 5.00 | 0.01023 | 33.07 ± 0.15 | 0.02 | 0.00 | 0.23 ± 0.03 | −15.83 ± 0.15 | 9, 12, 16, 17 |
| 2003E | 2452635.00 ± 7.00 | 0.01470 | 34.01 ± 0.28 | 0.04 | 0.00 | 0.11 ± 0.03 | −15.85 ± 0.31 | 9, 12 |
| 2003bl | 2452700.00 ± 3.00 | 0.01432 | 34.07 ± 0.30 | 0.02 | 0.00 | 0.19 ± 0.02 | −15.42 ± 0.31 | 9, 12 |
| 2003fb | 2452777.00 ± 6.00 | 0.01756 | 34.36 ± 0.15 | 0.16 | 0.00 | 0.45 ± 0.10 | −15.48 ± 0.16 | 9, 12 |
| 2003hl | 2452869.00 ± 5.00 | 0.00818 | 32.16 ± 0.10 | 0.06 | 0.00 | 0.43 ± 0.04 | −15.76 ± 0.13 | 9, 10, 12 |
| 2004fx | 2453304.00 ± 4.00 | 0.00886 | 32.71 ± 0.15 | 0.09 | 0.00 | 0.18 ± 0.04 | −15.46 ± 0.16 | 9 |
| 2005ay | 2453453.50 ± 3.00 | 0.00270 | 31.15 ± 0.40 | 0.02 | 0.08 | 0.19 ± 0.03 | −16.32 ± 0.40 | 2, 10 |
| 2005cs | 2453549.50 ± 1.00 | 0.00154 | 29.39 ± 0.47 | 0.03 | 0.01 | 0.19 ± 0.01 | −15.03 ± 0.47 | 2, 3, 5, 6, 8, 10, 16 |
| 2006bp | 2453834.50 ± 0.50 | 0.00351 | 31.42 ± 0.45 | 0.03 | 0.40 | 0.53 ± 0.02 | −17.63 ± 0.46 | 4, 5, 8, 16 |
| 2008bk | 2454543.40 ± 6.00 | 0.00077 | 27.89 ± 0.23 | 0.02 | 0.00 | 0.13 ± 0.02 | −15.12 ± 0.23 | 7, 9, 16 |
| 2009ib | 2455041.80 ± 3.10 | 0.00435 | 30.32 ± 0.45 | 0.03 | 0.13 | 0.17 ± 0.02 | −15.01 ± 0.45 | 11 |
| 2018lab | 2458481.40 ± 1.00 | 0.00920 | 32.75 ± 0.40 | 0.07 | 0.15 | 0.13 ± 0.05 | −15.00 ± 1.27 | 13, 15 |
| 2022acko | 2459918.67 ± 1.00 | 0.00526 | 31.39 ± 0.33 | 0.03 | 0.03 | 0.35 ± 0.03 | −15.40 ± 0.33 | 14, 15 |

**Note.** The explosion dates and errors are taken from the listed references.

**References.** (1) Hamuy (2001); (2) Tsvetkov et al. (2006); (3) Brown et al. (2007); (4) Quimby et al. (2007); (5) Dessart et al. (2008); (6) Pastorello et al. (2009); (7) Van Dyk et al. (2012); (8) Brown et al. (2014); (9) Anderson et al. (2014a); (10) Faran et al. (2014); (11) Takáts et al. (2015); (12) Galbany et al. (2016); (13) Pearson et al. (2023); (14) Bostroem et al. (2023); (15) Gaia Photometric Science Alerts; (16) Sternberg Astronomical Institute Supernova Light Curve Catalog: http://www.sai.msu.su/sn/sncat/; (17) VSNET: http://www.kusastro.kyoto-u.ac.jp/vsnet/index.html.

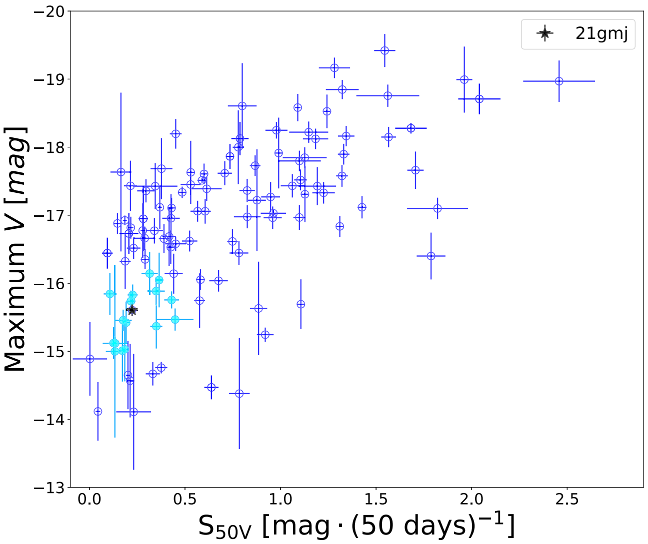

**Figure 3.** $V$-band light-curve slope vs. maximum $V$-band magnitude scatterplot for a sample of SNe II (see Valenti et al. 2016). The black star is SN 2021gmj and the cyan data points show the 16 nearest SNe that we use for photometric comparison. Properties and references for the literature sample can be found in Table 3.

Figure 4. SN 2021gmj is the bluest in color evolution, consistent with the low reddening found from the EW of the Na I D lines. Because of this, throughout this paper we adopt a total reddening of $E(B-V)_{\rm total} = 0.05 \pm 0.01$ mag, as well as an extinction law with $R_V = 3.1$ (Cardelli et al. 1989).

## 4. Host-galaxy Properties

NGC 3310 is a starburst galaxy with a peculiar morphology, showing shell/bow structures and a prominent circumnuclear starburst ring. This galaxy has been extensively studied from X-ray to radio wavelengths. From these studies we know that NGC 3310 has been part of at least a single minor merger, which triggered a burst of star formation that has lasted 10–100 Myr (Elmegreen et al. 2002). This merger enriched the NGC 3310 disk with low-metallicity gas, producing an oxygen abundance of $12 + \log({\rm O/H}) \approx 8.2 - 8.4$ dex in the disk and circumnuclear region (Pastoriza et al. 1993; Wehner et al. 2006; Hägele et al. 2010; Miralles-Caballero et al. 2014). This translates to subsolar metallicity in the range between 0.3 and 0.5 $Z_\odot$ (assuming solar abundances from Asplund et al. 2009).

NGC 3310 was observed as part of the PPAK Integral Field Spectroscopy Nearby Galaxies Survey (PINGS; Rosales-Ortega et al. 2010); details about the observations and reductions are given by Miralles-Caballero et al. (2014). The three-pointing mosaic has a spatial sampling of 1 arcsec$^2$ spaxel$^{-1}$ and the field of view fully covers the SN 2021gmj explosion site. The spatial resolution is dominated by the physical size of the fibers, which translates to a resolution of 2.″7 (more details can be found in Sánchez et al. 2016). A map of the H$\alpha$ emission of NGC 3310 is shown in Figure 5. To study the properties of the SN 2021gmj explosion site, we follow the method presented in several previous works (e.g., Galbany et al. 2016, 2018). The key output of the analysis pipeline is a stellar-continuum-subtracted emission-line spectrum of the SN region. The region has a physical size of ∼86 × 86 pc$^2$ on the 1 arcsec$^2$ spaxel (i.e., linear scale of 86 pc arcsec$^{-1}$).

From the spectrum we can obtain key properties of the ionized gas surrounding the SN explosion site. In Table 4 we show the values obtained for the star formation rate density ($\Sigma$(SFR)), EW of H$\alpha$ (EW(H$\alpha$)), reddening as measured by the Balmer decrement, and three different oxygen abundance measurements from the N2, O3N2, and D16 calibrations (Marino et al. 2013; Dopita et al. 2016, for the N2 and O3N2 and D16 calibrations, respectively). Both the SFR intensity and EW(H$\alpha$) show the starburst character of the host, with $\Sigma$(SFR) being in the top 20% of the PISCO sample (Galbany et al. 2018) and with the EW(H$\alpha$) measurement being the second

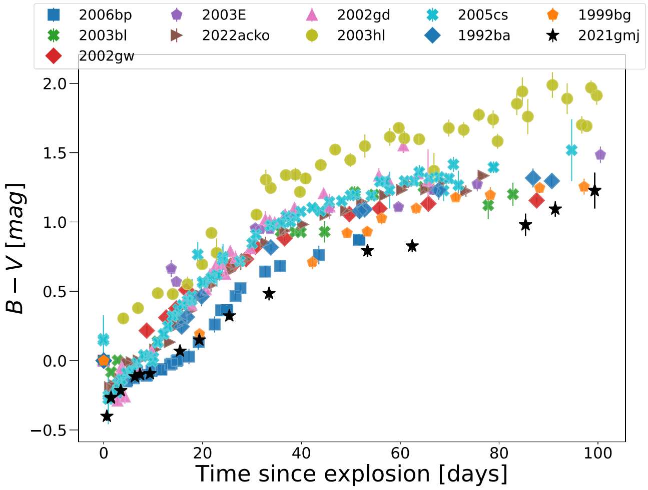

**Figure 4.** $B - V$ color evolution of SN 2021gmj compared with other SNe II from the literature. All data have been corrected for host and Milky Way reddening. SN 2021gmj is bluer than the overall sample.

highest of the whole sample. All of our measurements of the oxygen abundance point to 0.4–0.5 times the solar value (Asplund et al. 2009), which is consistent with previous measurements (Pastoriza et al. 1993; Miralles-Caballero et al. 2014). Our measured value belongs to the lowest 30% of the PISCO sample. The reddening is higher than our measured value for SN 2021gmj. This may be explained by the larger region probed by a single spaxel at the SN 2021gmj location, which may have on average a higher reddening than the direct line of sight toward SN 2021gmj.

## 5. Distance with the Expanding Photosphere Method

The distance to NGC 3310 has available measurements using calibrations of the Tully–Fisher (TF) relationship (de Vaucouleurs et al. 1981; Bottinelli et al. 1984; Giraud 1985; Bottinelli et al. 1986; Tully & Fisher 1988). The most recent TF distance is 18.7 Mpc ($\mu = 31.36 \pm 0.40$ mag; Tully & Fisher 1988). While the TF relationship works well for most spiral galaxies, the intrinsic scatter makes the distance to a single galaxy inaccurate (Czerny et al. 2018). Thus, to better constrain the distance to NGC 3310, we use the EPM originally developed by Kirshner & Kwan (1974). The EPM is based on a similar method employed for pulsating variable stars from Baade (1926) and assumes that the photosphere is homologously expanding. We can obtain the distance from the relation

$$t = D\left(\frac{\theta}{v_{\rm phot}}\right) + t_0, \tag{2}$$

with $D$ the distance, $v_{\rm phot}$ the photospheric velocity, $\theta$ the angular size of the photosphere, and $t_0$ the explosion epoch. Similar to the methodology of previous work (Hamuy et al. 2001; Leonard et al. 2003; Dessart & Hillier 2005; Jones et al. 2009), the photometry can be combined to write the residuals

$$\epsilon = \sum_{v\in S} \frac{\{m_v - A_v + 5\log_{10}[\theta\xi(T_c)] - b_v(T_c)\}^2}{(\sigma_v^2 + \sigma_{A_v}^2)}, \tag{3}$$

which, after minimizing these residuals, allow us to simultaneously derive the color temperature ($T_c$) and angular size ($\theta$). Here, $\xi$ is the dilution factor, $b_v$ is the synthetic magnitude obtained from a blackbody at temperature $T_c$, $A_v$ is the extinction, $m_v$ is the observed magnitude, and $S$ is the filter set. The corresponding uncertainties for the magnitude and extinction are $\sigma_v$ and $\sigma_{A_v}$, respectively. Here we use the dilution factors from Jones et al. (2009).

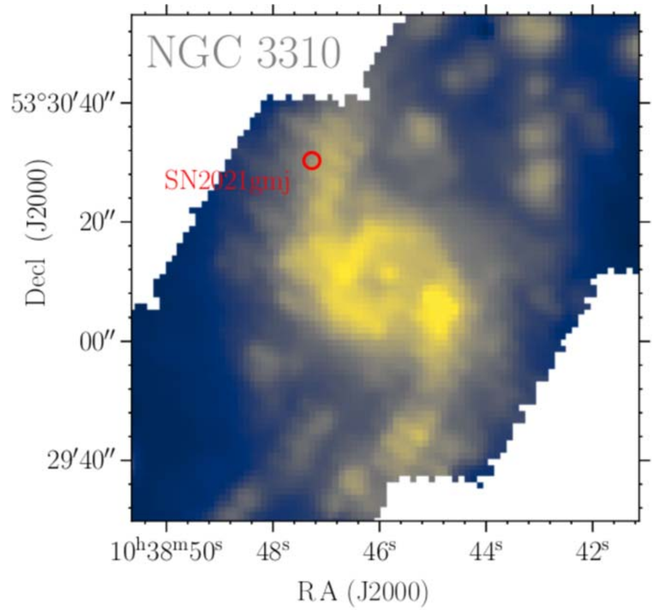

**Figure 5.** Continuum-corrected Hα emission map of NGC 3310. The position of SN 2021gmj is indicated with a red circle. The linear scale corresponds to 86 pc arcsec$^{-1}$.

**Table 4**
Local Properties of the Ionized Gas near SN 2021gmj as Derived from PINGS Integral Field Unit Data, Together with the PISCO Sample Means for Comparison (See Section 4)

| Property | Value | Unit | PISCO Mean[a] |
|---|---|---|---|
| Σ(SFR) | $0.065 \pm 0.001$ | $M_\odot$ yr$^{-1}$ kpc$^{-2}$ | 0.013 |
| $E(B-V)$ | $0.20 \pm 0.02$ | mag | … |
| EW(Hα) | $289.2 \pm 0.3$ | Å | 37.4 |
| 12 + log O/H (N2) | $8.5 \pm 0.1$ | dex | … |
| 12 + log O/H (O3N2) | $8.43 \pm 0.07$ | dex | … |
| 12 + log O/H (D16) | $8.40 \pm 0.07$ | dex | 8.65 |

**Note.**
[a] If published.

For this work we use the filter set *BVI*. To obtain *I* magnitudes from our *ri* magnitudes we use the Lupton color transformations.[23] The photospheric velocity is estimated by measuring the velocity at maximum absorption of Fe II λ5169. Later than approximately 50 days after explosion the relation between $\theta/v$ and $t$ becomes nonlinear (Jones et al. 2009), so we limit ourselves to epochs < 50 days from explosion. SN 2021gmj spectroscopy has five epochs in this range where the Fe II λ5169 velocity was measured by fitting polynomials to the absorption profile of the Fe II feature. To obtain photometric measurements at each velocity epoch, we do a simple linear interpolation. We implemented a Markov Chain Monte Carlo (MCMC) code using the Python library `emcee`

---

[23] https://www.sdss3.org/dr8/algorithms/sdssUBVRITransform.php#Lupton2005

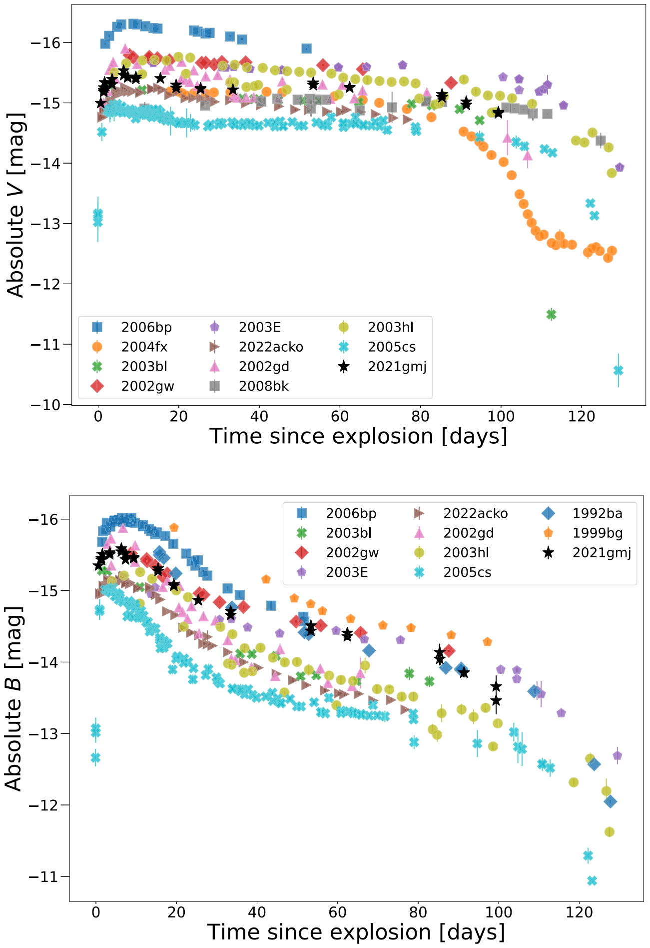

**Figure 6.** Top: *V* light curve of SN 2021gmj compared to a sample of similar SNe II. Bottom: same for the *B* band. All light curves show absolute magnitudes, and are dereddened from both Galactic and host extinction. The bluer than average colors of SN 2021gmj can be explained by the brighter *B* magnitude compared to the sample after ∼50 days.

(Foreman-Mackey et al. 2013), which uses the residuals in Equation (3) as the log-likelihood together with uniform priors on $\theta$ and $T_c$. To estimate the optimal parameters of Equation (2) (i.e., the distance and explosion epoch), we use our MCMC code with uniform priors on the explosion epoch $t_0$ and distance $D$. We use a wide prior for $t_0$, which covers 5 days before and 0.5 day after our initial guess: $t_0 = 2459293.28$ JD. Finally, we use a uniform prior between 0 and 100 Mpc in distance. We obtain a distance of $17.8^{+0.6}_{-0.4}$ Mpc and an explosion epoch consistent with our initially assumed value estimated in Section 2. This distance is consistent with the TF distances available in the literature. For the remainder of this paper we adopt a distance of $17.8^{+0.6}_{-0.4}$ Mpc to SN2021gmj and therefore to NGC 3310.

## 6. Photometric Evolution

The full multiband light curves of SN 2021gmj are shown in Figure 2. The light-curve evolution resembles that of other LL SNe II (Figure 3; Gall et al. 2015; Valenti et al. 2016). Our early detection and immediate high-cadence follow-up observations capture the multiband light-curve rise of 8.4 days in the *V* band, reaching a maximum brightness of $M_V = -15.45$ mag. Following maximum, the light curve plateaus for about 100 days, with an average slope of 0.004 mag per 50 days in the *V* band. At the end of the plateau SN 2021gmj drops in brightness by 2 mag in the optical bands. After the fall from the plateau, the light curve settles into the radioactive tail, with a roughly constant slope until our observations stopped around 400 days after explosion.

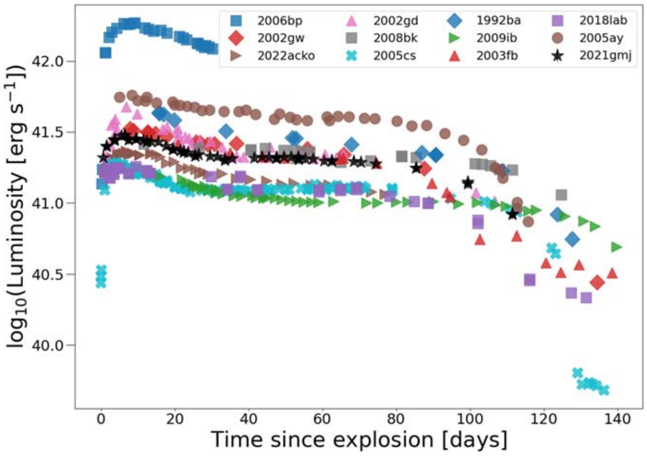

**Figure 7.** *BVri*/*BVRI* pseudobolometric light curves of SN 2021gmj and SNe from the photometric comparison sample, including the more-luminous SN 2006bp. SN 2021gmj fits the average luminosity of the LL SN II sample quite well. The plateau of near 100 days is also expected for this LL class.

A comparison of the SN 2021gmj *B* and *V* light curves with those of other SNe II taken from our comparison sample is shown in Figure 6. The relatively bluer color of SN 2021gmj (see Figure 4) is explained by the *B*-filter brightness which is above the sample average after midplateau. The bluer color is also consistent with the weaker iron lines that we describe in Section 9. Blue colors have also been associated with CSM interaction in luminous SNe II (Polshaw et al. 2016; Rodríguez et al. 2020).

### 6.1. Pseudobolometric Light Curve

We construct the *BVri* pseudobolometric light curve for SN 2021gmj through numerical integration of the spectral energy distribution (SED) and compare it with the *BVri* or *BVRI* pseudobolometric light curves of our comparison sample; see Figure 7. Despite the blue colors of SN 2021gmj, the bolometric luminosity is similar to the comparison sample in both plateau length and brightness, most closely matching SN 2008bk, SN 2002gw, and SN 2002gd.

## 7. Nickel Mass

During the nebular phase, the light curve is powered by the radioactive decay of $^{56}$Ni → $^{56}$Co → $^{56}$Fe. We calculate the nickel mass of SN 2021gmj by constructing a pseudobolometric light curve from our *Vri* photometry 200–400 days past explosion. The *B* observations do not have a large enough signal-to-noise ratio to detect the SN in the nebular phase. In addition we choose to not include the *g* band as we need to compare to SN 1987A, which does not have Sloan filter photometry. In addition, we performed several tests to confirm that excluding the *B*/*g* bands do not significantly affect our pseudobolometric light curve and nickel mass calculation (A. Bostroem et. al. 2024, in preparation). We then, following Spiro et al. (2014), compare this integrated luminosity with the pseudobolometric luminosity of SN 1987A in the same bands and epoch. To obtain the Sloan filter photometry for SN 1987A, we performed synthetic photometry using published optical spectra. With the pseudobolometric luminosity at each epoch, $L_{\rm pbol}$, we fit the following model to obtain the nickel mass ($M_{^{56}{\rm Ni}}$)

$$\frac{L_{\rm pbol}(t)}{L_{\rm pbol}^{87A}(t)} = \left(\frac{M_{^{56}{\rm Ni}}}{0.075}\right)\left(\frac{1-\exp(-(T_0/t)^2)}{1-\exp(-(540/t)^2)}\right), \tag{4}$$

where $t$ is the time in days after explosion, 0.075 is the nickel mass of SN 1987A in solar mass units, and $T_{0,87A} = 540$ days is the gamma-ray trapping timescale for SN 1987A (Jerkstrand 2011). This model assumes that the energy deposition of cobalt decay is diluted by the exponential factor $(1 - \exp(-(T_0/t)^2))$ (Clocchiatti & Wheeler 1997). The two parameters of the model, the nickel mass ($M_{^{56}{\rm Ni}}$) and trapping timescale ($T_0$), are fitted with an MCMC sampling. We use flat priors from 0 to 1 $M_\odot$ and from 0 to 1000 days for $M_{^{56}{\rm Ni}}$ and $T_0$, respectively. The MCMC chain gives the following means and errors, where the systematic error in $M_{^{56}{\rm Ni}}$ is given by the uncertainty in distance modulus: $M_{^{56}{\rm Ni}} = 0.014 \pm 0.001$ $M_\odot$ and $T_0 = 653^{+207}_{-131}$ days are the most probable values. This nickel mass value is consistent with an LL SN II (e.g., Valenti et al. 2016), although it is not as extreme as other SNe with very low-energy explosions (e.g., SN 2005cs $\sim 10^{-3}$ $M_\odot$; Spiro et al. 2014). The ejected nickel is also higher than some SNe from higher-mass progenitors with fallback (Zampieri et al. 2003).

## 8. Early Light-curve Modeling

### 8.1. Shock-cooling Models

The shock-cooling models of Sapir & Waxman (2017) have been used to characterize the early light-curve properties of CCSNe (e.g., Hosseinzadeh et al. 2018, 2023; Andrews et al. 2019; Dong et al. 2021; Tartaglia et al. 2021; Shrestha et al. 2024). These models have been updated in recent work (Morag et al. 2023) where an interpolation between the planar and spherical phases of expansion is used together with a parameter calibration against hydrodynamic models with a diverse range of progenitor properties. It also includes analytical prescriptions that take into account deviations from a blackbody SED. We follow the prescription of Hosseinzadeh et al. (2018), and use the MCMC routine implemented in the "light-curve fitting" package (Hosseinzadeh & Gomez 2020), to constrain the progenitor radius and to identify if shock cooling is the only energy source in the early light-curve evolution of SN 2021gmj.

We use our multiband UV plus optical light curve up to 15 days postexplosion to fit for the model. The model assumes a uniform density core and an $n = 3/2$ polytrope envelope suitable for an RSG. An MCMC routine is used to fit for the model parameters: the progenitor radius ($R$), the shock velocity scale ($v_{s*}$), the envelope mass ($M_{\rm env}$), the product of the total ejecta mass ($M$), and a constant of order unity ($f_\rho$, hereafter "scaled ejecta mass" ($f_\rho M$)), and the time of explosion ($t_0$). Flat priors are assumed for each parameter (see Hosseinzadeh et al. 2018 for a complete description of the codes and assumptions used), and in the case of the explosion epoch we take a flat prior −3.0 days to 0 day from discovery. The resulting posterior distributions and fits are shown in Figure 8.

The best-fit radius of $5.8^{+0.2}_{-0.2} \times 10^{13}$ cm $\approx 834$ $R_\odot$ is consistent with typical RSG radii (Levesque et al. 2005). Other parameters of the model ($M_{\rm env}$, $f_\rho M$, and $v_{s*}$) cannot be directly compared with the progenitor and explosion properties as these parameters depend on the density structure of the progenitor, which is controlled by the parameter $f_\rho$ and not constrained by the model. The model fits neither the UVOT bands nor the optical bands. In particular the UV bands of the model underestimate the emission. Although the discrepancy is not high considering the light-curve dispersion, this may be an indication that the early emission requires an extra source of energy (Hosseinzadeh et al. 2018; Dong et al. 2021; Pearson et al. 2023; Shrestha et al. 2024). Other signs of the struggle of the model to do a proper fit are seen in Figure 8, where we show how the model is inconsistent with our nondetections by pushing the explosion epoch to lower values. This can be interpreted as the inability of the model to have a fast rise; it has also been interpreted as evidence of CSM interaction in previous work. In the next section we will find more evidence for the presence of material surrounding the progenitor of SN 2021gmj.

### 8.2. Hydrodynamic Modeling of the Light Curves with SNEC

To further constrain the progenitor properties, and to understand if any contribution of the early-time light curve is coming from CSM interaction, we use the open source 1D hydrodynamic code, SuperNova Explosion Code (`SNEC`; Morozova et al. 2015). `SNEC` takes as input a progenitor model (density, temperature, velocity, etc.), an explosion energy $E$, a nickel mass, and a nickel mass outer boundary. Following Morozova et al. (2017), we fix the nickel mass boundary up to 5 $M_\odot$ as this weakly affects the light curve. We also fix the nickel mass to be $M_{^{56}{\rm Ni}} = 0.014 \pm 0.001$ (stat) $\pm$ 0.001(sys) $M_\odot$ as obtained in Section 7.

To convert the bolometric properties of the model to broadband photometry, we assume a blackbody SED. As the actual spectra of SNe show significant line blanketing from metal lines, a blackbody fit is not appropriate for short wavelengths. Owing to this we exclude filters bluer than $g$. We also do not include the $V$ band as it overlaps significantly with the $g$ and $r$ wavelength ranges.

As done by Morozova et al. (2018) and Dong et al. (2021), we use a two-step approach to fit our *gri* optical light curves. We use the solar metallicity progenitor models of Sukhbold et al. (2016), which were calculated with the stellar evolution code `KEPLER` (Weaver et al. 2017). We first constrain the explosion energy $E$ and progenitor mass $M$ by fitting the plateau between 27 and 112 days after explosion. These dates correspond to the end of the initial slope (Anderson et al. 2014a; Valenti et al. 2016) and the end of our data during the fall from the plateau. We consider only RSG progenitors, using models with masses in the range 9–15 $M_\odot$ in steps of 0.5 $M_\odot$ and 17, 19, and 21 $M_\odot$. Our grid of explosion energies ranges from 0.01 to 0.5 foe, with 20 points equally spaced, and we add four equally spaced points from 0.6 to 1.4 foe. We define the best-fit $E$ and $M$ as the parameters which minimize the $\chi^2$ value over all three bands considered at all epochs. The model with the lowest $\chi^2$ has $M = 10$ $M_\odot$ and $E = 0.294$ foe, although we remark that the models can fit with a similar probability using both a lower mass and smaller explosion energy.

After fixing $E$ and $M$, we explore the influence of CSM by superimposing a steady wind on the original density profile. This wind extends from the progenitor radius $R_*$ up to a

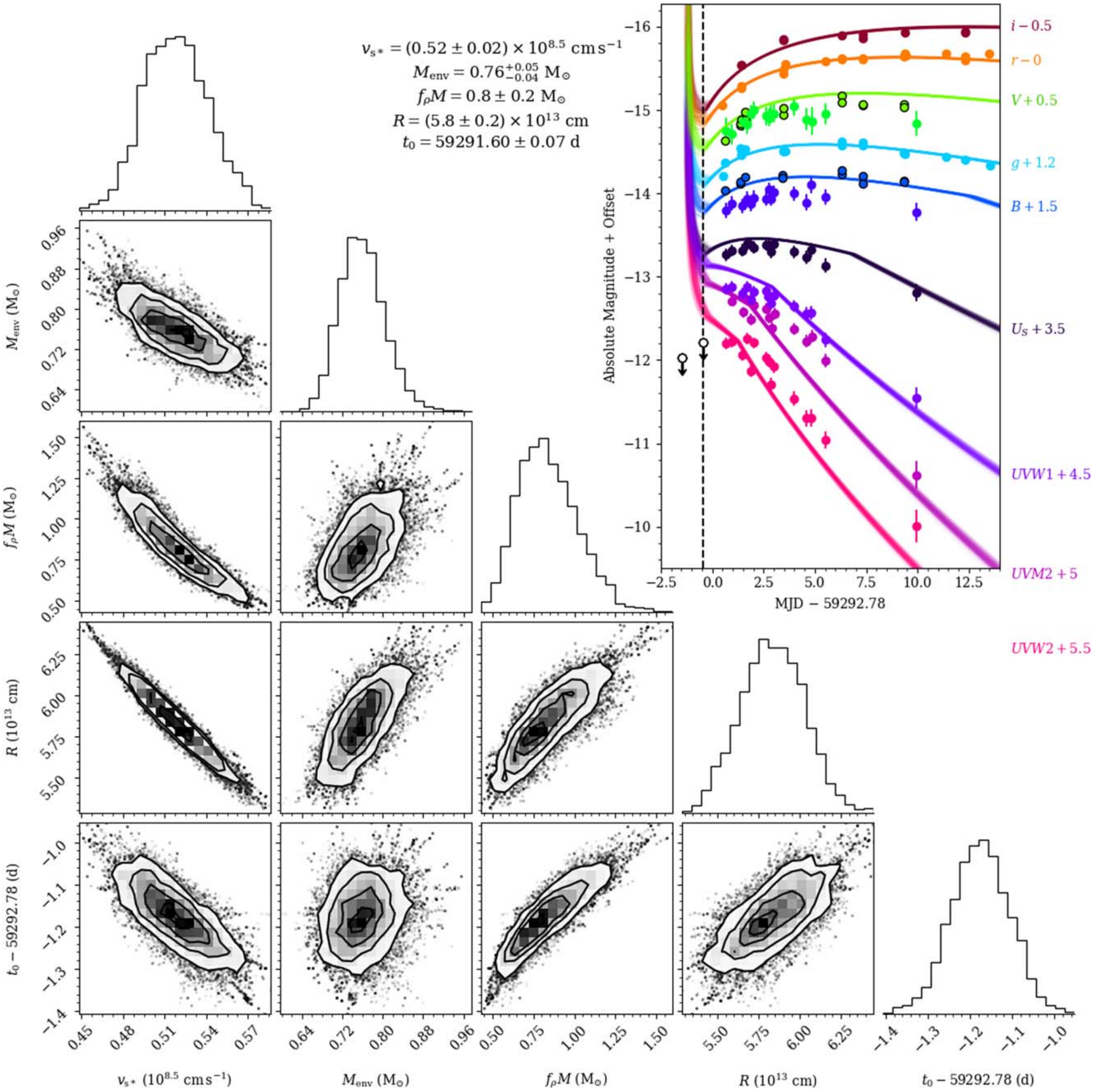

**Figure 8.** Posterior probability distributions for the progenitor radius $R$, shock velocity scale ($v_{s*}$), envelope mass ($M_{\rm env}$), scaled ejecta mass ($f_\rho M$), and time of explosion ($t_0$). The top-right panel shows a sample of model light curves using randomly selected parameters drawn from the posterior, together with the observed magnitudes. The last two nondetections are also shown with white circles, and a dashed line also shows the last nondetection for clarity. The resulting median and 1$\sigma$ errors for the best-fit parameters are listed at the top of the figure. The model does not fit well the UV bands and it violates our nondetections, indicating that the model is not able to fit the fast rise in the light curves. We interpret this as evidence of CSM interaction.

radius $R_{\rm CSM}$

$$\rho(r) = K/r^2;\ R_* \leqslant r < R_{\rm CSM}, \tag{5}$$

where $K$ is the line density that can also be written as $K = \dot{M}/v_\infty$, where $\dot{M}$ is the mass-loss rate and $v_\infty$ is the velocity of the CSM. We run models with an outer CSM radius between 500 and 1200 $R_\odot$ in steps of 50 $R_\odot$ and density from $0.2 \times 10^{13}$ g cm$^{-1}$ to $15 \times 10^{13}$ g cm$^{-1}$ in steps of 0.2 g cm$^{-1}$. We again calculate the reduced $\chi^2$ value for each model to obtain the best-fit parameters, but this time we only compare the light curve between the explosion epoch and the end of the light-curve slope break ($s_1$ phase) at 26.72 days. In Figure 9 we show the surface plot of the $\chi^2$ values in our $R$–$K$ parameter space. Our best-fit model has $K = 2.4 \times 10^{13}$ g cm$^{-1}$ and $R = 750\ M_\odot$, and there is a clear degeneracy between both parameters. This has been observed in previous work (e.g., Morozova et al. 2018) and indicates that the model more strongly constrains the total CSM mass, which is a product of $K$ and $R_{\rm CSM}$ in this simple model

$$M_{\rm CSM} = \int_{R_*}^{R_{\rm CSM}} 4\pi\rho r^2 dr = 4\pi K (R_{\rm CSM} - R_*). \tag{6}$$

The total CSM mass of our best-fit model is $M_{\rm CSM} = 0.025\ M_\odot$. This CSM mass is lower than those in the sample of

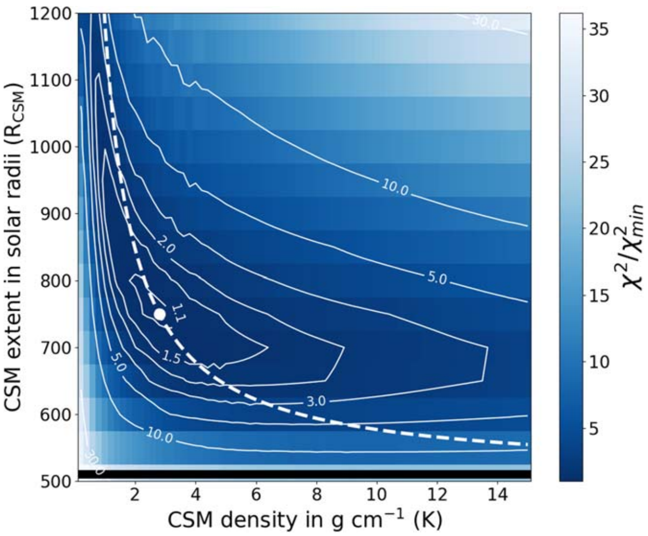

**Figure 9.** $\chi^2$ surface plot for the CSM models as discussed in Section 8.2. The best-fit parameters are marked with a white dot, which corresponds to a density of $K = 2.4 \times 10^{17}$ g cm$^{-1}$ and a CSM radial extent of $R = 750\ R_\odot$. Contour lines are also shown and the black thick line denotes the progenitor extent without CSM (510 $R_\odot$, `KEPLER` model). There is a clear degeneracy between both parameters, which was also observed in other works (e.g., Morozova et al. 2017). The degeneracy follows closely the curve where the CSM mass is constant (white-dashed line in the plot), at a value of $M_{\rm CSM} = 0.025\ M_\odot$ at the best fit.

Morozova et al. (2018; without considering the lower limits), but it seems to follow the observed trends for a low-mass and low-energy explosion. Although the CSM mass is low, its importance for the early light curve is evident in Figure 10, where we show the light curves of the models with and without CSM. The fit in the $g$ and $r$ bands improves significantly owing to the excess early emission coming from the ejecta–CSM interaction. However, the $i$-band model does not show a proper fit. This indicates that although the hydrodynamic modeling that includes CSM is an improvement, our simplified treatment of the model SED and our steady-wind assumption for the mass loss maybe not be a good representation of the density profile of the immediate vicinity of the progenitor of SN 2021gmj.

## 9. Spectroscopic Evolution

### 9.1. Overall Evolution

The optical spectroscopic evolution of SN 2021gmj is shown in Figure 11. The earliest spectra exhibit a blue continuum with broad H$\alpha$ emission and little absorption. These early-time spectra show no signs of prominent, narrow emission lines—sometimes referred to as flash features—often seen in SNe II hours to a few days after explosion (e.g., Bruch et al. 2021). There is strong and broad emission around 4600 Å instead. Further analysis of this emission in the early spectra and implications are discussed in Section 9.5.

Over time the SN becomes redder and the P Cygni profiles of the hydrogen features become more prominent. Starting with the spectrum taken 13 days past explosion, Fe II $\lambda$5169 is observed and can be used to trace the photosphere. Around 20 days past explosion, more Fe-group lines appear, namely Fe II $\lambda\lambda$5267, 5363. At 20 days we also see the emergence of the Ca II NIR triplet around 8500 Å. In Figure 12, we show SN 2021gmj spectra in the region near H$\alpha$. 50 days past explosion there is evidence of an absorption feature blueward of H$\alpha$. At this phase, this feature is identified as high-velocity (HV) H$\alpha$ and is attributed to a dense shell that forms due to the interaction of CSM with the SN ejecta (Chugai et al. 2007; Gutiérrez et al. 2014). With this interpretation we measure a velocity of ∼8100 km s$^{-1}$ for this feature.

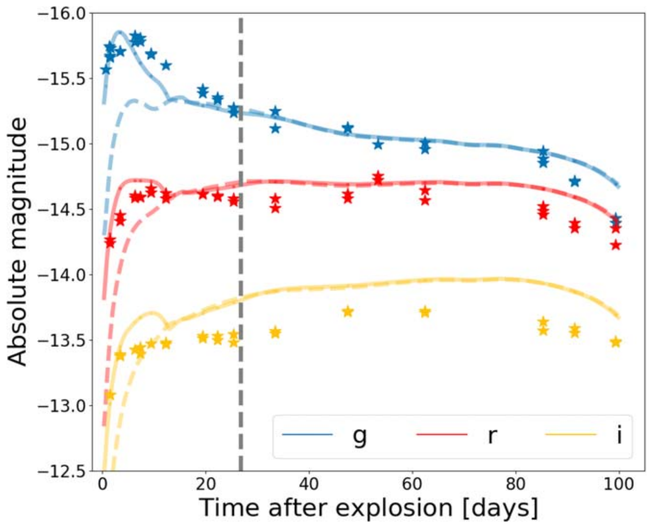

**Figure 10.** Best CSM model fit compared to SN 2021gmj *gri* light curves. The best fit (solid lines) corresponds to a density of $K = 2.4 \times 10^{17}$ g cm$^{-1}$ and a CSM radial extent of $R = 750\ R_\odot$. We also show the model without CSM using dashed lines. The vertical dashed line marks the end of the $s_1$ phase, which is used as the earliest epoch in the progenitor mass–explosion energy fits and the latest epoch in the CSM parameter fit. We can see that adding CSM improves the fit significantly at early epochs.

After the fall from the plateau, we obtained three spectra at 204, 229, and 402 days past explosion, which we show in Figure 13. They exhibit a clear transition from a P Cygni-dominated spectrum to an emission-line nebular spectrum where we can observe the growing strength of forbidden lines like [O I], [Fe II], and [Ca II]. The presence of nebular emission lines tells us that the expanding ejecta have become optically thin. This marks the end of the photospheric phase of the SN. These emission lines will be used in Section 10 to constrain the progenitor mass and yields.

### 9.2. Metallicity of the Supernova

Anderson et al. (2014a) have shown that the EW of the Fe II $\lambda$5018 line can be used to constrain the metallicity of SNe II. In our spectra at 50 days we measured the Fe II $\lambda$5018 line EW; its value of 12 Å is closest to the $0.4Z_\odot$ measurement from the models used by Anderson et al. (2016). This measurement is in agreement with the host oxygen abundance determinations of 0.4–0.5 solar described in Section 4.

### 9.3. Comparison with Other Type II Supernovae

It is well established that expansion velocities are correlated with luminosity for SNe II in general (Hamuy 2003; Kasen & Woosley 2009). In particular, LL SNe II are expected to have low expansion velocities during the plateau, but there are counterexamples in the literature (Dastidar et al. 2019; Rodríguez et al. 2020). We now wish to establish a spectral comparison of SN 2021gmj with a range of SNe II and see how well it fits to known correlations.

Figure 14 shows the spectrum of SN 2021gmj at 16 days past explosion compared to other LL SNe II at similar phases:

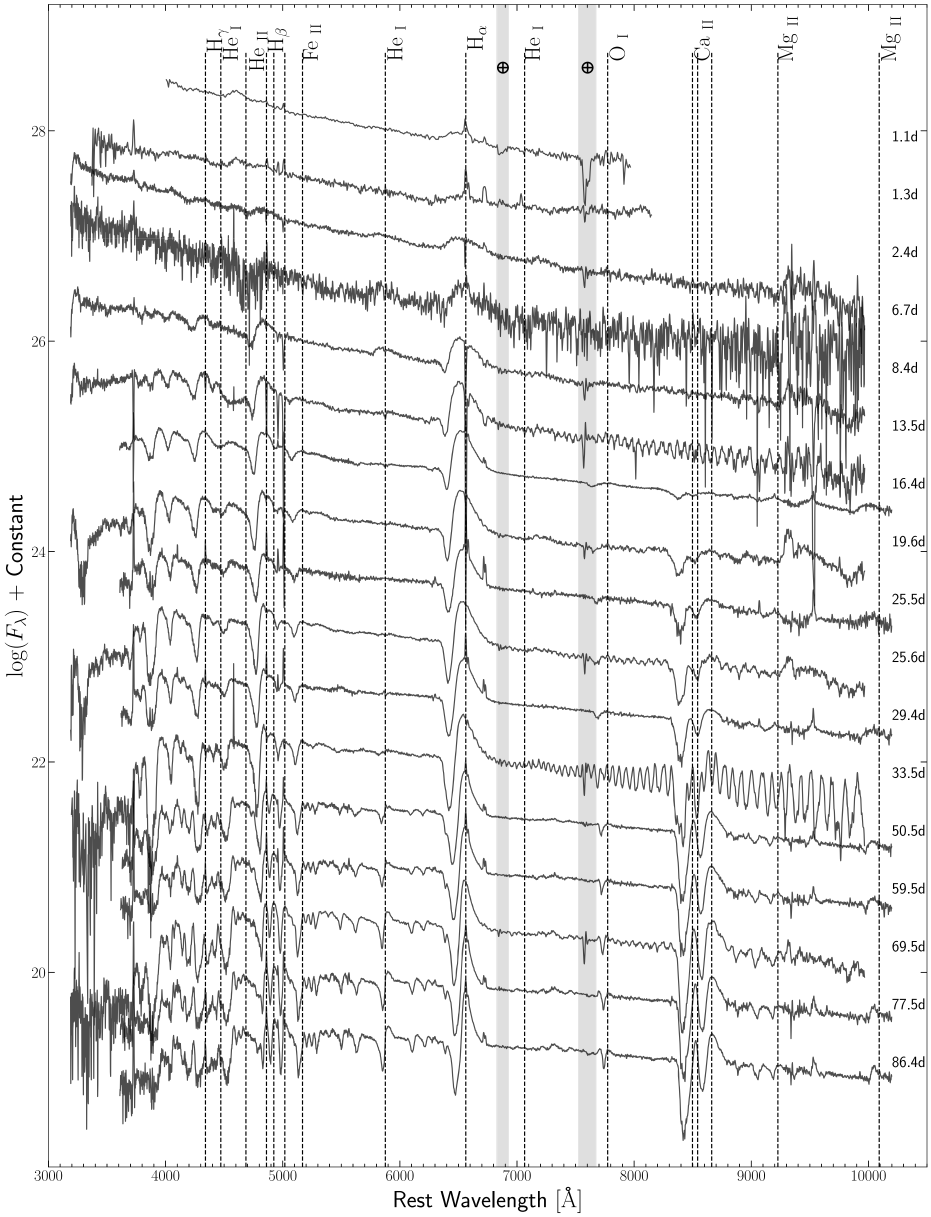

**Figure 11.** Optical spectral evolution of SN 2021gmj in the photospheric phase. The phase of each observation, in days since explosion, is labeled for each spectrum. The gray vertical bands with the ⊕ symbol mark the regions of strongest telluric absorption. The dashed vertical lines mark the rest wavelengths of the Balmer lines of hydrogen along with other elements. The day 33.54 spectrum suffers from bad fringing at near-infrared (NIR) wavelengths; fringing is also visible in the day 13.54 spectrum.

SN 2005cs (Pastorello et al. 2006) and SN 2010id (Gal-Yam et al. 2011). The epoch of 16 days was chosen to compare to the other objects at a very similar phase when the Hα P Cygni profiles are well developed. We also include SN 2006bp (Quimby et al. 2007) for reference as a more-luminous SN II with broader lines. The shallow and narrow absorption of Hα and Hβ in the SN 2021gmj spectrum is most similar to SN 2010id. At this stage, many lines like Na I D and the Ca II NIR triplet have not developed yet, unlike in the LL SN II 2005cs.

Figure 14 also shows the day 50 spectrum of SN 2021gmj compared with the same sample at similar phases. The line profiles are narrow, consistent with what is expected from an LL SNe II. Metal lines also appear relatively shallow, consistent with the subsolar metallicity measurement. The lower velocity of the lines allows the triplet emission of Ca II in the red part of the spectrum to be visible. We also observe the appearance of Ba II and Sc II lines, which are common in the colder spectra of LL SNe II (Pastorello et al. 2004; Spiro et al. 2014). Although SN 2021gmj shows narrower lines compared to SN 2006bp, the absorption lines are not as deep as in SN 2005cs, and the Ba II λ6497 line that distorts Hα in SN 2005cs is not visible. This suggests that SN 2021gmj has intermediate spectral characteristics between the more extremely underluminous end of LL SNe II and brighter SNe II.

### 9.4. Expansion Velocities

The expansion velocity evolution of SN 2021gmj is shown in Figure 15 along with the average velocity values for a

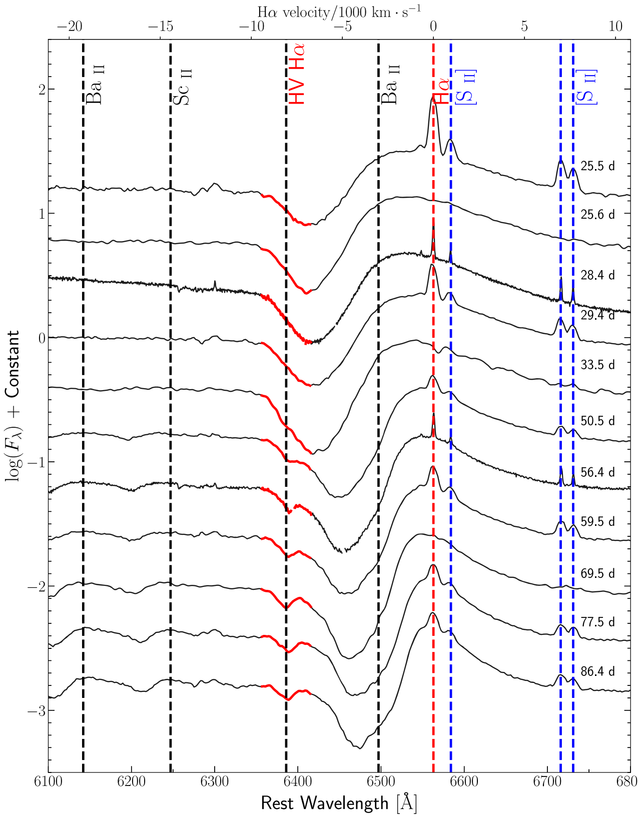

**Figure 12.** Spectral time series of SN 2021gmj showing the evolution near the Hα line. We highlight the wavelength positions of Ba II and Sc II in black; we also label with blue font the wavelengths of host-galaxy nebular lines which contaminate the SN spectra. These narrow lines most likely originate from a nearby star-forming region. In red we mark Hα together with the absorption component that we label as HV Hα at ∼8000 km s$^{-1}$.

sample of SNe II (Gutiérrez et al. 2017). At early times, 5–10 days past explosion, SN 2021gmj has Hα and Hβ velocities of ∼8000–10,000 km s$^{-1}$, slightly higher than normal for an LL SN II (Pastorello et al. 2004; Spiro et al. 2014) and slightly lower than the average sample of Gutiérrez et al. (2017). The Hα expansion velocities of SN 2021gmj decline more rapidly than the average sample to ∼7000 km s$^{-1}$ at 20 days past explosion, which is more consistent with what is seen in LL SNe II. In the lower-right panel of Figure 15, which compares the Fe II 5169 Å velocities, we also include measured velocities from LL SNe II from the following literature: SN 1999br (Pastorello et al. 2004), SN 2002gd and SN 2003Z (Spiro et al. 2014), SN 2005cs (Pastorello et al. 2009), and SN 2009N (Takáts et al. 2014). SN 2021gmj exhibits below-average velocities with respect to the overall SN II population, but in the higher range compared to other LL SNe II.

### 9.5. Early-time Spectra and Flash Signatures

As discussed in Section 9 and shown in Figure 16, the early spectra of SN 2021gmj have a broad emission feature around 4600 Å. Similar features have been described as "ledge-shaped," and may arise from a blend of high-ionization lines (see, e.g., Bruch et al. 2021). Although in other works the ledge feature is referred to as a flash feature, in this work we choose to call it a ledge to differentiate this broad emission with the narrow ones observed in very early spectra of SNe II. Past work has also analyzed this feature in other SNe II. Quimby et al. (2007) suggest that the ledge could be due to either He II λ4686 or an N II λλ4480, 4630 blend. If this emission was caused by N II, then N II λλ5490, 5680 should also be visible (Dessart & Hillier 2005); however, this line is absent from our early spectra of SN 2021gmj. Similar to the argument with the N II line, one can look for transition lines of other elements which can be comparable in brightness at high temperatures. In the case of C and N this is challenging because there are strong nearby lines such as Hδ or He I.[24]

Following Quimby et al. (2007), as the ejecta cool and He recombines, the He II λ4686 would become depopulated while He I λ5876 would grow stronger. This is precisely what we see in SN 2021gmj (Figure 16), suggesting that the early-time emission is due to blueshifted He II λ4686 and that the ejecta are still highly ionized at these phases. If this feature is associated with He II, it has a velocity of 4000 ± 100 km s$^{-1}$ as measured by fitting a Gaussian and a linear continuum in the region. This value is not unreasonable compared with other SNe. In SNe II, P Cygni emission maxima are expected to be blueshifted at early times by as much as 5000 km s$^{-1}$ (Dessart & Hillier 2005; Anderson et al. 2014b). However, the amount of blueshift is correlated with the slope of the V-band light curve at 30 days (Anderson et al. 2014b). There we see that flatter light curves have smaller blueshifts. This would imply a blueshift of ∼1000 km s$^{-1}$ for the peak of the P Cygni profiles in the spectra of SN 2021gmj 30 days after explosion; extrapolating to early phases, we expect a blueshift of ∼2000–3000 km s$^{-1}$. Indeed, looking at Hα in SN 2021gmj, the emission appears blueshifted by no more than 3000 km s$^{-1}$. Thus, it seems unlikely that the He II λ4686 blueshift would be as high as 4000 km s$^{-1}$.

To place SN 2021gmj in context, we compare the early-time spectra with spectra from a sample of LL SNe II that show emission near He II λ4686 (Figure 17). We also included the normal-luminosity SN 2006bp, which was one of the first SNe II with very early spectra showing flash features. The explosion epochs, redshifts, and references for this comparison sample can be found in Table 5. In the LL SNe II, the ledge feature peaks near the high-ionization lines of C III, N III, and possibly N V λ4604. SN 2006bp, however, is brighter and has broader features than the other LL SNe II, having the peak near O III lines. We observe that no SN shows a feature with a peak near the rest frame of He II λ4686. A relevant observation is that the blueshift of the ledge feature, if we interpret it as He II λ4686, is inconsistent with the blueshift of Hα in all of the spectra shown. Despite their mismatched velocities, this feature could still be interpreted as He II λ4686 if there is an ionization stratification of the ejecta. If higher-velocity material is at higher ionization than the rest of the slower ejecta, the ionized He II lines may be observed at a higher velocity than the Balmer lines. The higher ionization at higher velocities can occur as CSM interaction of the HV ejecta is exposed to the hard radiation from the ejecta–CSM shock region. A similar argument is found in the recent work of Chugai & Utrobin (2024). The authors propose that the He II λ4686 emission comes from dense fragments embedded in the forward-shock region that undergo Rayleigh–Taylor instabilities. We conclude that while the ledge feature seems common in LL SNe II (Pearson et al. 2023), we cannot definitively identify its origin.

---

[24] In the case of N V (in LTE conditions), one expects N IV emission near 4100 Å at $k_BT = 1.6$–1.7 eV. In the case of C III, there is a strong C IV line very close to 5800 Å at a temperature of $k_BT \approx 1.2$ eV. We do not observe any of these transitions.

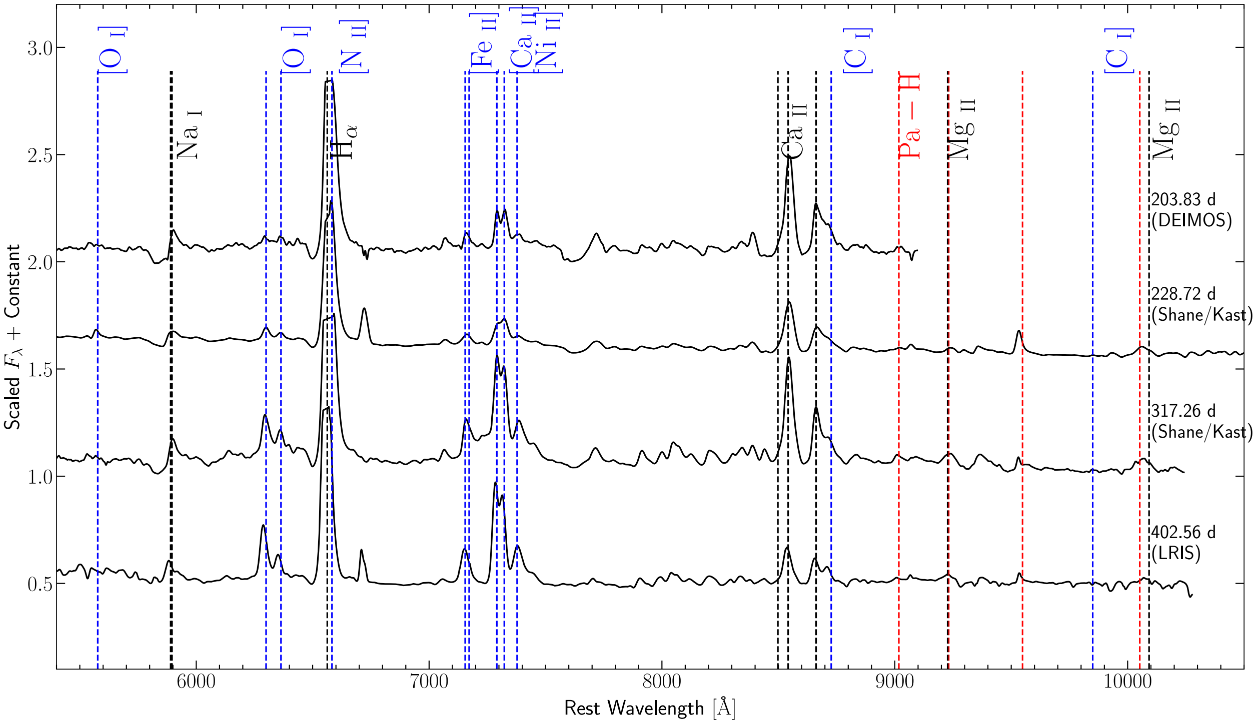

**Figure 13.** Spectroscopic sequence of SN 2021gmj in the nebular phase. In dashed lines we mark the wavelength of important allowed transitions (black), forbidden transitions (blue), and the Paschen series in the NIR (red). Near 6700 Å there is likely an artifact coming from a bad subtraction of host emission from [S II].

To further understand the origin of the early emission, we compare the first spectrum of SN 2021gmj with the model spectra from Dessart et al. (2017; Figure 18). These models explode 15 $M_\odot$ RSG progenitors with different density structures, controlled by differing mass-loss rates and atmospheric scale heights. The r1w1 and r2w1 models have progenitor radii of $R_* = 501\ R_\odot$ and $R_* = 1107\ R_\odot$, respectively, and a mass-loss rate of $\dot{M} = 10^{-6}\ M_\odot\ \mathrm{yr}^{-1}$ for both. Model r1w1h has an extended atmospheric density scale height of 0.3 $R_*$ up to a density of $10^{-12}$ g cm$^{-3}$ followed by a power law with exponent 12 until it reaches the density profile of a $\dot{M} = 10^{-6}\ M_\odot\ \mathrm{yr}^{-1}$ wind at a radius of $\sim 2 \times 10^{14}$ cm. Finally, model r1w5h is similar to r1w1h but with a scale height of 0.1 $R_*$, which then decreases to a wind of $\dot{M} = 5 \times 10^{-3}\ M_\odot$ yr$^{-1}$ and finally to a wind of $\dot{M} = 10^{-6}\ M_\odot\ \mathrm{yr}^{-1}$ at a radius of $\sim 2 \times 10^{14}$ cm.

These two extended-envelope models (r1w1h and r1w5h) attempt to represent the complex extended atmospheres observed in RSGs, which can have inflows/outflows and inhomogeneities up to a few stellar radii (Arroyo-Torres et al. 2015; Kervella et al. 2016; Goldberg et al. 2022; González-Torà et al. 2022; Humphreys & Jones 2022). To do the comparison we first convolve the model spectra with a Gaussian with a width equal to the instrumental resolution of the SN 2021gmj spectrum, and bin the models to the resolution of the observations. We then fit a blackbody to the continuum of both the model and our observed spectrum and normalize each spectrum. Like SN 2018lab (Pearson et al. 2023), SN 2021gmj is better fit by the extended-atmosphere models (r1w1h and r1w5h). In the r1w1h and r1w5h models, the initially strong and narrow He II λ4686 and N V λ4604 emission profiles blend together to create a broader profile centered around 4600 Å, which is similar to the 4600 Å feature seen in SN 2021gmj.

Following Dessart et al. (2017), the broad diversity of the emission in early-time spectra can be explained by the origin of the broadening of these high-ionization lines. If the line of a given element is formed in a slow wind of unshocked material the line profile is symmetric, driven by incoherent electron scattering. Later, when the dense wind is swept up by the SN ejecta, a dense shell forms that will have as a spectral profile a Doppler broadened and blueshifted emission peak (Dessart et al. 2017). This scenario seems consistent with the early observations of LL SNe II. Therefore, although we cannot rule out the HV He II origin of this feature, the spectral evolution is consistent with a progenitor exploding into a higher-density material.

## 10. Progenitor Mass through Nebular Spectral Analysis

As the plateau phase ends, the photosphere recedes from the hydrogen-rich outer layers and we are able to observe emission from the core. This allows us to constrain the elemental composition of the inner layers of the ejecta and the progenitor mass. In particular, the emission from the forbidden lines of [O I] is a good probe of the oxygen mass in the ejecta and therefore to the MS mass of the star (Woosley & Weaver 1995). We use the nebular spectra models from Jerkstrand et al. (2012, J12 models hereafter) to constrain the progenitor mass of SN 2021gmj. These models explode 12, 15, and 19 $M_\odot$ single-star progenitors with a piston, giving a total of 1.2 foe of kinetic energy, and fix the mass of the Fe/He zone to give a nickel mass of 0.062 $M_\odot$.

In Figure 19, we compare our Keck/LRIS observation at ∼400 days past explosion with the J12 models. To identify which model best characterizes the overall spectrum of SN 2021gmj, we normalize the model spectra to the total flux over the observed wavelength range of SN 2021gmj (5500–10000 Å). This has the effect of aligning the continuum

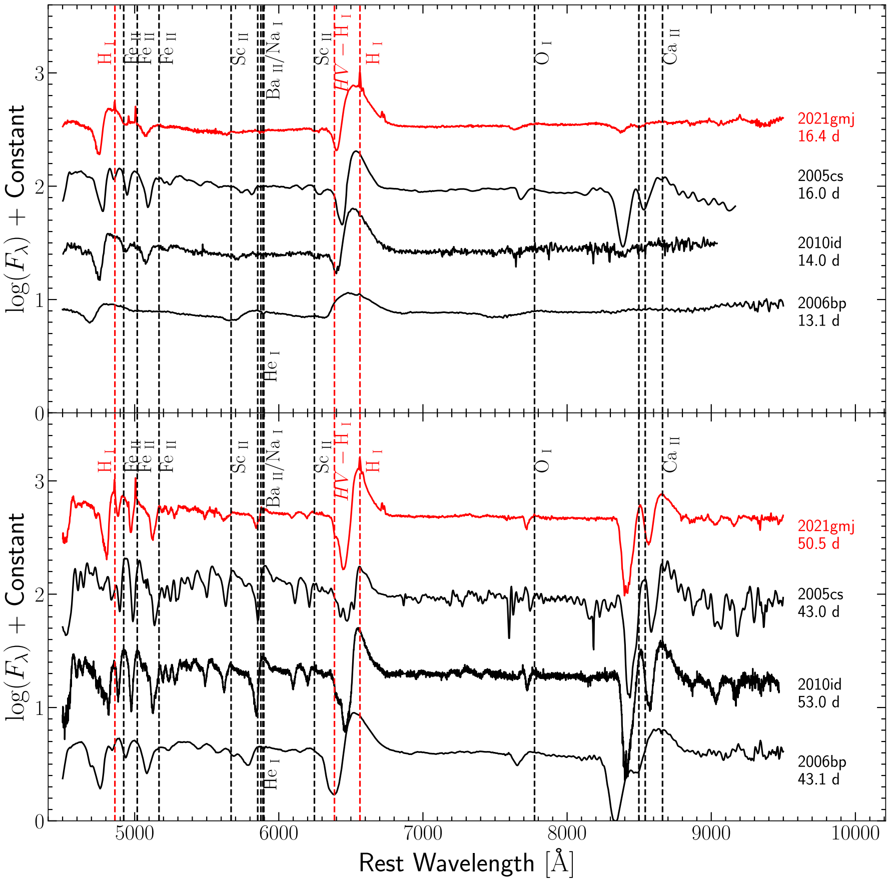

**Figure 14.** The upper panel shows a comparison of SN 2021gmj with other LL SNe II and SN 2006bp around 15 days past explosion. SN 2021gmj is most similar to SN 2010id, with weak and narrow H$\alpha$ absorption and missing blue lines. The lower panel displays a comparison with other LL SNe II around 50 days past explosion. The line profiles are narrow, consistent with what is expected from LL SNe II. SN 2006bp is included as an example of a more ordinary SN II where the line profiles are broader. All the spectra have been normalized after a blackbody fit. SN 2021gmj has intermediate spectral characteristics between the LL end of LL SNe II and more energetic SNe II.

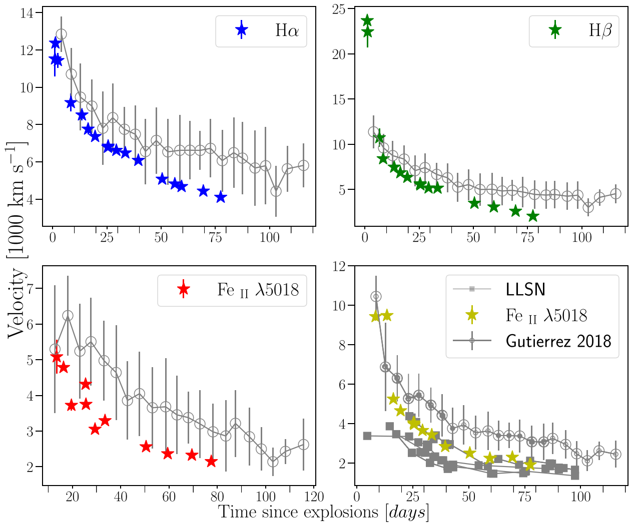

**Figure 15.** Expansion velocities as a function of phase for SN 2021gmj (star data points). The average and 1$\sigma$ range values of a large sample of SNe II from Gutiérrez et al. (2017) are also shown (gray open circles). In the lower-right plot we include the measured velocities of LL SNe II from the literature. SN 2021gmj exhibits below-average velocities with respect to the overall SN II population, but are in the higher range when compared to other LL SNe II.

regions, allowing us to compare the observed and model spectra. Overall, the models have broader lines than SN 2021gmj. The width of the lines is related to the velocity of the inner layers, which correlates with the explosion energy. Additionally, the small line width allows us to distinguish the [Ni II] $\lambda$7378 and [C I] $\lambda$8727 emission clearly. We can therefore conclude that SN 2021gmj has a lower explosion energy than these models, consistent with our `SNEC` modeling.

Next we consider in detail the emission of specific lines and discuss the progenitor mass. As mentioned, the emission from [O I] is related to the progenitor mass. We measured the integrated flux of the [O I] doublet by fitting Gaussian profiles over a flat continuum for SN 2021gmj and the model spectra. The luminosity (or flux) is then normalized by the cobalt-decay power at 400 days to obtain the fraction of oxygen luminosity relative to cobalt decay. This fraction is 0.22 for SN 2021gmj and is equivalent to the model of 12 $M_\odot$ within the uncertainties (~5%–10% assuming that the distance is the main source of statistical uncertainty).

Some authors prefer to measure the ratio of [O I] to [Ca II] as this can minimize the effects of extinction, distance, and cobalt decay, allowing a better comparison of SNe to each other (Elmhamdi 2011; Kuncarayakti et al. 2015; Fang & Maeda 2018; Fang et al. 2019, 2022; Hiramatsu et al. 2021a, 2021b). We estimate the ratio for SN 2021gmj, measuring the flux of the

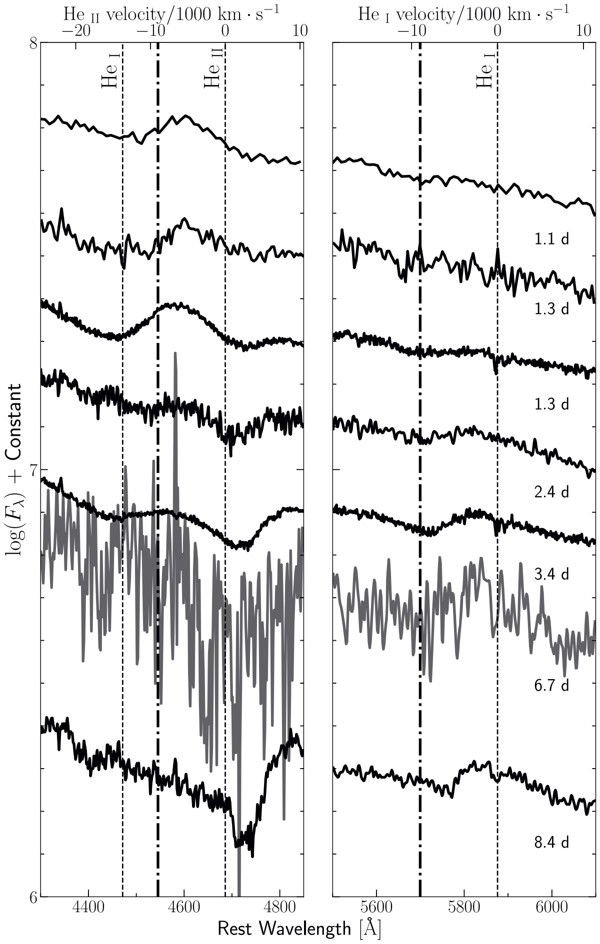

**Figure 16.** Comparison of the early-time blue emission, likely due to He II λ4686 (left panel), to that of He I λ5876 (right panel). As He II becomes weaker (i.e., the He recombines), the He I λ5876 feature becomes stronger.

[Ca II] λλ7291, 7323 doublet as we did with [O I]. In the case of [Ca II], to avoid overestimating the flux we also include in our fit the visible neighboring lines [Fe II] λλ7155, 7453 and [Ni II] λλ7378, 7412 as extra Gaussians profiles to the fitting model. We measure J12 model line ratios following the same procedure as well. The measured luminosity ratio [O I]/[Ca II] = 1/2 corresponds to the value of the 12 $M_\odot$ model.

A relevant consideration when comparing SN 2021gmj to these nebular models is the mismatch in nickel mass, where the model has a factor of ∼4.5 more nickel than SN 2021gmj itself. While the empirical scaling accounts for the difference in flux due to the differences in Ni mass, the increasing nickel mass in the models increases the ionization and electron density, which can suppress forbidden-line emission. In particular, Ca and O forbidden lines can be relatively weaker for higher nickel mass values (Dessart & Hillier 2020). We expect that our measurement using the ratio of these lines can alleviate at least partially this uncertainty.

Dessart & Hillier (2020) observe that [Ca II] can be a very efficient coolant, such that an increased Ca mass fraction in the oxygen shell will cause the [O I] emission to be quenched. This quenching would cause us to underestimate the progenitor mass. However, the mixing of O and Ca shells is expected to occur in higher progenitor masses ($\gtrsim$17 $M_\odot$); as we find that the progenitor mass of SN 2021gmj is well below 17 $M_\odot$, this is unlikely to affect our results. All our analyses assume that the progenitor of SN 2021gmj is a single star and that the mass-loss history of the progenitor is normal when compared to the assumed expected values used in J12 (Nieuwenhuijzen & de Jager 1990 parameterization is used in that work).

Our analysis allows us to conclude that SN 2021gmj has a progenitor mass of $M_{\rm ZAMS} \approx 12$ $M_\odot$, and a nickel mass and explosion energy compatible with a less massive progenitor. This result is further supported by the hydrodynamic modeling of the light curves, which gave a progenitor mass of 10 $M_\odot$ and an explosion energy of 0.294 foe.

**Table 5**
Type II Supernovae with a Broad 4600 Å Feature in Early-time Spectra

| Name | Explosion Date | $z$ | References |
|---|---|---|---|
| SN 2002gd | 2452553.0 (4.0) | 0.007 | Anderson et al. (2014a) |
| SN 2005cs | 2453549.5 (1.0) | 0.001 | Pastorello et al. (2006), Silverman et al. (2017) |
| SN 2006bp | 2453834.5[a] | 0.0035 | Quimby et al. (2007) |
| SN 2010id | 2455454.5 (2.0) | 0.017 | Gal-Yam et al. (2011) |
| ASASSN-14jb | 2456946.6 (3) | 0.006 | Meza et al. (2019) |
| SN 2018lab | 2458481.40 (1.0) | 0.00920 | Pearson et al. (2023) |

**Note.** The explosion dates and uncertainties are taken from the listed references.

[a] No uncertainty in the explosion epoch given by Quimby et al. (2007).

## 11. Discussion

In Section 8, our light-curve modeling suggests the presence of CSM around the progenitor of SN 2021gmj. Here we will analyze additional evidence supporting or disputing the presence of CSM interaction for SN 2021gmj.

There are two spectroscopic observations that may support the CSM scenario: the HV Hα in the plateau spectra and the early emission near 4600 Å. The HV Hα can be explained by the presence of a wind. As discussed by Chugai et al. (2007), either the unshocked wind or the cold dense shell that forms in the ejecta–wind interaction will have an increased opacity in material at high velocities due to the X-ray emission originating in the reverse and forward shocks.

Coming back to the early emission, our analysis in Section 9.5 points to either the presence of HV He II and/or high-ionization lines of C and N. Similar conclusions were obtained for other SNe II. The study of SN 2018fif (Soumagnac et al. 2020) showed very early, low-resolution spectra with hints of emission of He II, N III–N V, and C IV. Similarly, SN 2016bkv (Hosseinzadeh et al. 2018) exhibited distinct double-peaked emission from C III/N III and He II up to 5 days after explosion. Finally, we mention SN 2021yja (Hosseinzadeh et al. 2022; Vasylyev et al. 2022), which also showed a multicomponent, ledge-like feature. Although SN 2021yja was in the bright class of SNe II, the progenitor mass constraint from preexplosion imaging put an upper limit of 9 $M_\odot$, which is closer to the progenitor mass of LL SNe II. As in the case of SN 2021gmj, the early emission of both SN 2018lab and SN 2021yja was most similar to the extended-atmosphere progenitor models from Dessart et al. (2017). This may be evidence that LL SNe II show spectral signatures of interaction in the very first days after explosion. The interaction may arise from the SN shock ramming through the low-density

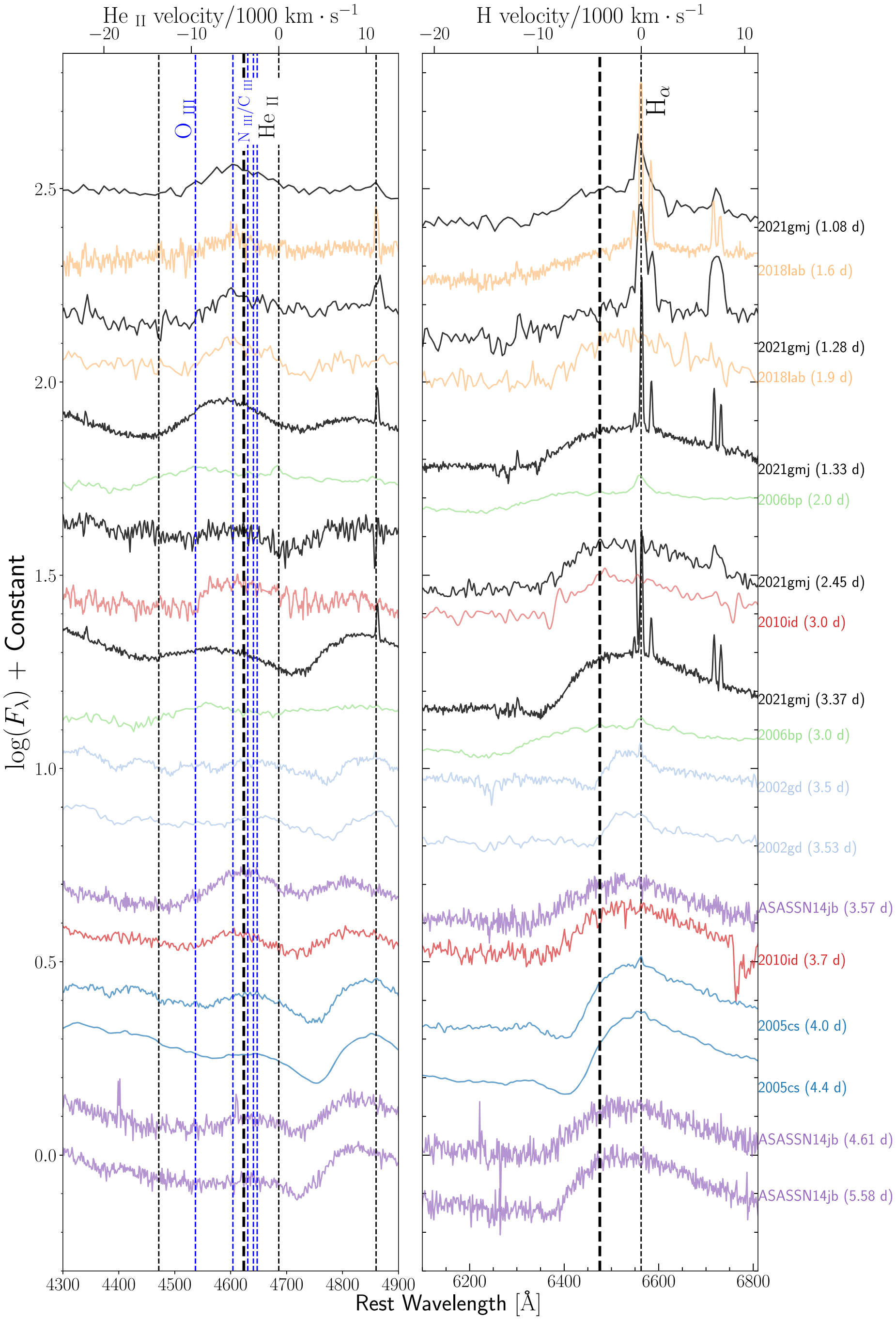

**Figure 17.** Comparison of the early emission in SN 2021gmj and other SNe with similar spectral profiles during the first 6 days after explosion, centered at He II λ4686 (left panel) and at Hα (right panel). In each panel the thick black dashed lines show the position of a blueshift of 4000 km s$^{-1}$ with respect to the rest wavelengths of He II λ4686 and Hα. Thin blue dashed vertical lines are drawn at the rest wavelengths of He II λ4686, N III, C III, O III, and H transitions. All spectra have been normalized to a blackbody fit. All SNe in the sample have emission near 4600 Å, indicating high ionization of the ejecta at early times. The explosion epochs, redshifts, and references for this comparison sample can be found in Table 5.

atmosphere of the RSG. Thereafter, the shock may encounter a wind of lower density, which may extend the duration of the spectral signatures. The ejecta–atmosphere/CSM interaction may increase the peak brightness, like in the case of SN 2021yja. Future studies of early interaction signatures would benefit from higher-resolution spectra, as the current resolution does not allow a definite answer regarding the origin of the 4600 Å line; it is possible that we may be observing other element transitions besides ionized He.

Both the light-curve modeling and the extended-star spectral models require a density of $\sim 10^{-10}$–$10^{-11}$ g cm$^{-3}$, a distance of just 1.5 times the progenitor-star radius. Whether this mass is associated with a high-density wind originating from a sudden increase in mass loss very near in time to the explosion (Quataert & Shiode 2012; Smith & Arnett 2014; Fuller 2017; Kuriyama & Shigeyama 2020), or whether the material is just an extended atmosphere (e.g., Mcley & Soker 2014; Soker 2021), is something to study in future work.

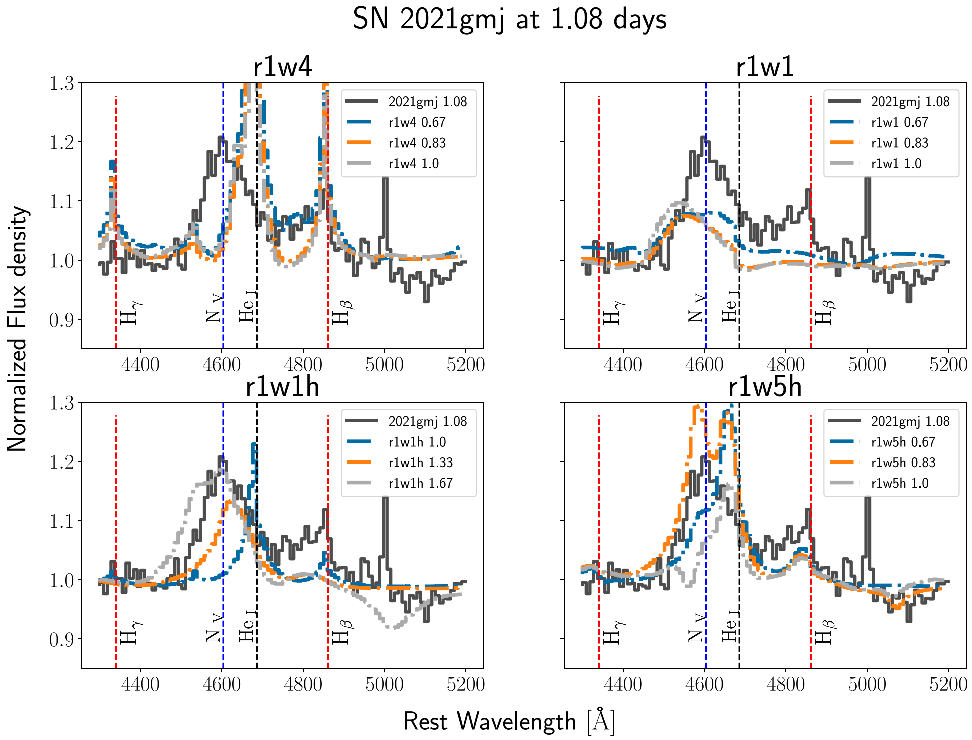

**Figure 18.** Comparison of the first spectrum of SN 2021gmj around 4600 Å with a selection of models from Dessart et al. (2017). Each panel compares to a given model at the three closest epochs. All spectra have been normalized to a blackbody continuum fit. The models have been convolved with a Gaussian with the width of the resolution of our observation (18 Å for the first LT spectra) and have been binned to match the observed resolution. In general, all models underestimate the H$\beta$ emission. SN 2021gmj is most similar to the extended-atmosphere models, r1w1h and r1w5h, just hours after the strong and narrow emission lines of He II $\lambda$4686 and N V $\lambda$4604 (black and blue dashed lines in the figure, respectively) evolve into a broader profile.

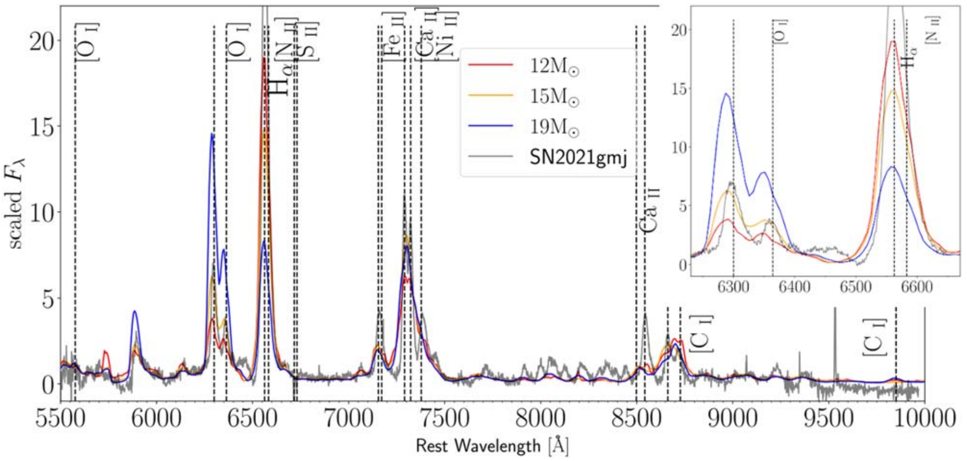

**Figure 19.** Spectra of SN 2021gmj (dereddened) at 402 days past explosion compared with the 12 $M_\odot$, 15 $M_\odot$, and 19 $M_\odot$ models from J12 at 400 days. Both the observed and model spectra have been normalized to the integrated flux in the 5500–10000 Å region. On the upper right we display an inset of the spectra around [O I] and H$\alpha$. Our analysis shows that the relative flux of the [O I] doublet to both the [Ca II] flux and to the cobalt-decay power is very close to the 12 $M_\odot$ model.

Murai et al. (2024) have recently published a study of SN 2021gmj. Their analysis greatly coincides with ours, obtaining a consistent peak brightness, expansion velocities, progenitor mass, and ejected nickel mass. A progenitor mass of 12 $M_\odot$ was obtained through a nebular spectral analysis similar to ours. They also used hydrodynamic models of progenitors with CSM, and obtained a mass-loss rate of $\sim 10^{-3}$–$10^{-2.5}$ $M_\odot$ yr$^{-1}$ with a progenitor of a fixed mass of 12 $M_\odot$. This mass-loss rate also agrees with our measurements. If we assume a terminal wind velocity of 10 km s$^{-1}$ like in Murai et al. (2024), we obtain a mass-loss rate of $\sim 3 \times 10^{-3}$ $M_\odot$ yr$^{-1}$. Our progenitor mass is potentially lower than the mass obtained by Murai et al. (2024). We trust the value from hydrodynamic simulations more than the one from the nebular analysis (12 $M_\odot$), so we did not fix the progenitor mass in our `SNEC` modeling (10 $M_\odot$). Both works do agree that the progenitor mass is not extremely low compared to more LL events like SN 2005cs (Maund et al. 2005). SN 2021gmj then, taking both studies, presents itself as moderate explosion in a moderate-mass RSG progenitor, very close to the brightness limit of the class of LL SNe II. This is in agreement with our current understanding of the progenitors of LL SNe II (Spiro et al. 2014). The luminosity of an SN II is expected to depend on the progenitor mass, while the early peak luminosity depends more directly on the progenitor radius (e.g., Young 2004; Rabinak & Waxman 2011) and the amount of CSM (e.g., Morozova et al. 2018). Thus observations of LL SNe II like SN 2021gmj, which show signs of CSM interaction, provide key information on the diversity of RSG explosions.

## 12. Conclusions

We have presented photometric and spectral observations of the SN II 2021gmj. It photometrically belongs to the class of LL SNe II, with a maximum brightness of $M_V = -15.45$ mag. SN 2021gmj presents a decline of <0.01 mag per 100 days on the plateau, which lasts about 100 days. Both the photometric and spectral comparison show that SN 2021gmj is similar to a sample of LL SNe II, including expansion velocities and bolometric luminosity. SN 2021gmj synthesized a moderate amount of radioactive nickel, $M_{^{56}\mathrm{Ni}} = 0.014 \pm 0.001$ $M_{\odot}$, which together with the low expansion velocities point to a moderate progenitor mass and explosion energy (Hamuy 2003; Sukhbold et al. 2016). This is confirmed through our analysis of the nebular emission lines; the line-intensity ratios are consistent with the 12 $M_{\odot}$ progenitor model. Overall the basic properties of SN 2021gmj derived in this work are consistent with the higher-luminosity end of LL SNe II and are in agreement with the continuous distribution of parameters of RSG explosions (Spiro et al. 2014; Valenti et al. 2016).

The early light-curve modeling favors the presence of CSM very close to the star, which translates to a small CSM mass in our simple steady-wind assumptions. The `SNEC` best fit gives a CSM mass of $M_{\mathrm{CSM}} = 0.025$ $M_{\odot}$ in addition to the progenitor mass of 10 $M_{\odot}$, which exploded with a moderate energy of $E = 0.294$ foe. The low CSM mass agrees with the early-time spectral features, which do not show any narrow emission with electron-scattering wings. Instead, we observe the presence of a probable blend of high-ionization emission lines of C, N, and HV He II. This indicates that the line-formation region is partially or completely swept up by the fast-moving ejecta so that the overall profile is similar to a broad and blueshifted P Cygni line. This is further supported by the similarity of a spectroscopic emission feature around 4600 Å in SN 2021gmj to radiative hydrodynamic spectroscopic simulations of extended stars with CSM. The presence of this broad feature in several LL SNe II suggests that interaction signatures may be common in this class.

Although an abundance of photometric and spectroscopic evidence exists for the presences of compact and low-density material surrounding the RSG progenitor of SN 2021gmj, further research is required to understand if LL SNe II with CSM signatures arise from extended RSGs or from RSGs that have an increase of mass loss in the final stages of stellar evolution.

## Acknowledgments

Time-domain research by the University of Arizona team and D.J.S. is supported by National Aeronautics and Space Administration (NASA) grant 80NSSC22K0167, National Science Foundation (NSF) grants AST-1821987, 1813466, 1908972, 2108032, and 2308181, and the Heising-Simons Foundation under grant #2020-1864. J.E.A. is supported by the International Gemini Observatory, a program of NSF's NOIRLab, which is managed by the Association of Universities for Research in Astronomy (AURA) under a cooperative agreement with the NSF, on behalf of the Gemini partnership of Argentina, Brazil, Canada, Chile, the Republic of Korea, and the United States of America. Research by Y.D., N.M., and S.V. is supported by NSF grants AST-1813176 and AST-2008108. The Las Cumbres group is supported by NSF grants AST-1911151 and AST-1911225. K.A.B. is supported by an LSSTC Catalyst Fellowship; this publication was thus made possible through the support of grant 62192 from the John Templeton Foundation to LSSTC. The opinions expressed in this publication are those of the authors and do not necessarily reflect the views of LSSTC or the John Templeton Foundation.

L.G. acknowledges financial support from the Spanish Ministerio de Ciencia e Innovación (MCIN), the Agencia Estatal de Investigación (AEI) 10.13039/501100011033, and the European Social Fund (ESF) "Investing in your future" under the 2019 Ramón y Cajal program RYC2019-027683-I and the PID2020-115253GA-I00 HOSTFLOWS project, from Centro Superior de Investigaciones Científicas (CSIC) under the PIE project 20215AT016, and the program Unidad de Excelencia María de Maeztu CEX2020-001058-M. The Las Cumbres group is supported by NSF grants AST-1911151 and AST-1911225. A.V.F.'s group is supported by the Christopher R. Redlich Fund, Alan Eustace (W.Z. is a Eustace Specialist in Astronomy), Briggs and Kathleen Wood (T.G.B. is a Wood Specialist in Astronomy), Gary and Cynthia Bengier, Clark and Sharon Winslow, Sanford Robertson (Y.Y. was a Bengier-Winslow-Robertson Postdoctoral Fellow), and many other donors.

We appreciate the expert assistance of the staffs at the observatories where the data were obtained. Some of the data presented herein were obtained at the W. M. Keck Observatory, which is operated as a scientific partnership among the California Institute of Technology, the University of California, and NASA. The Observatory was made possible by the generous financial support of the W. M. Keck Foundation. A major upgrade of the Kast spectrograph on the Shane 3 m telescope at Lick Observatory, led by Brad Holden, was made possible through gifts from the Heising-Simons Foundation, William and Marina Kast, and the University of California Observatories. Research at Lick Observatory is partially supported by a generous gift from Google. This paper is based on observations made with the MuSCAT3 instrument, developed by the Astrobiology Center and under financial supports by JSPS KAKENHI (JP18H05439) and JST PRESTO (JPMJPR1775), at Faulkes Telescope North on Maui, HI, operated by the Las Cumbres Observatory. Some observations reported here were obtained at the MMT Observatory, a joint facility of the University of Arizona and the Smithsonian Institution.

This work used the Weizmann Interactive Supernova Data Repository (WISeREP; https://wiserep.weizmann.ac.il; Yaron & Gal-Yam 2012). This research has made use of the NASA/IPAC Extragalactic Database (NED, https://ned.ipac.caltech.edu/), which is operated by the Jet Propulsion Laboratory, California Institute of Technology, under contract with NASA. This work was performed in part at Aspen Center for Physics, which is supported by National Science Foundation grant PHY-2210452.

*Facilities:* ADS, MMT (Binospec), LCOGT (Sinistro, FLOYDS, MuSCAT3), Keck:I (LRIS), Keck:II (DEIMOS), Asiago:Copernico (Afosc), Shane (KAST), CTIO:PROMPT, Swift (UVOT), NED.

*Software:* astropy (Astropy Collaboration et al. 2013, 2018), corner (Foreman-Mackey 2016), emcee (Foreman-Mackey et al. 2013), FLOYDS pipeline (Valenti et al. 2014), `HOTPANTS` (Becker 2015), `lcogtsnpipe` (Valenti et al. 2016), MatPLOTLIB (Hunter 2007), NumPy (Harris et al. 2020), Scipy (Virtanen et al. 2020), and `SNEC` (Morozova et al. 2015).

## ORCID iDs

Nicolás Meza-Retamal https://orcid.org/0000-0002-7015-3446
Yize Dong (董一泽) https://orcid.org/0000-0002-7937-6371
K. Azalee Bostroem https://orcid.org/0000-0002-4924-444X
Stefano Valenti https://orcid.org/0000-0001-8818-0795
Lluís Galbany https://orcid.org/0000-0002-1296-6887
Jeniveve Pearson https://orcid.org/0000-0002-0744-0047
Griffin Hosseinzadeh https://orcid.org/0000-0002-0832-2974
Jennifer E. Andrews https://orcid.org/0000-0003-0123-0062
David J. Sand https://orcid.org/0000-0003-4102-380X
Jacob E. Jencson https://orcid.org/0000-0001-5754-4007
Daryl Janzen https://orcid.org/0000-0003-0549-3281
Michael J. Lundquist https://orcid.org/0000-0001-9589-3793
Emily T. Hoang https://orcid.org/0000-0003-2744-4755
Samuel Wyatt https://orcid.org/0000-0003-2732-4956
Peter J. Brown https://orcid.org/0000-0001-6272-5507
D. Andrew Howell https://orcid.org/0000-0003-4253-656X
Megan Newsome https://orcid.org/0000-0001-9570-0584
Estefania Padilla Gonzalez https://orcid.org/0000-0003-0209-9246
Craig Pellegrino https://orcid.org/0000-0002-7472-1279
Giacomo Terreran https://orcid.org/0000-0003-0794-5982
Vladimir Kouprianov https://orcid.org/0000-0003-3642-5484
Daichi Hiramatsu https://orcid.org/0000-0002-1125-9187
Saurabh W. Jha https://orcid.org/0000-0001-8738-6011
Nathan Smith https://orcid.org/0000-0001-5510-2424
Joshua Haislip https://orcid.org/0000-0002-6703-805X
Daniel E. Reichart https://orcid.org/0000-0002-5060-3673
Manisha Shrestha https://orcid.org/0000-0002-4022-1874
F. Fabián Rosales-Ortega https://orcid.org/0000-0002-3642-9146
Thomas G. Brink https://orcid.org/0000-0001-5955-2502
Alexei V. Filippenko https://orcid.org/0000-0003-3460-0103
WeiKang Zheng https://orcid.org/0000-0002-2636-6508
Yi Yang https://orcid.org/0000-0002-6535-8500

## References

Anderson, J. P., Dessart, L., Gutierrez, C. P., et al. 2014b, MNRAS, 441, 671
Anderson, J. P., González-Gaitán, S., Hamuy, M., et al. 2014a, ApJ, 786, 67
Anderson, J. P., Gutiérrez, C. P., Dessart, L., et al. 2016, A&A, 589, A110
Andrews, J. E., Sand, D. J., Valenti, S., et al. 2019, ApJ, 885, 43
Arroyo-Torres, B., Wittkowski, M., Chiavassa, A., et al. 2015, A&A, 575, A50
Asplund, M., Grevesse, N., Sauval, A. J., & Scott, P. 2009, ARA&A, 47, 481
Astropy Collaboration, Price-Whelan, A. M., Sipőcz, B. M., et al. 2018, AJ, 156, 123
Astropy Collaboration, Robitaille, T. P., Tollerud, E. J., et al. 2013, A&A, 558, A33
Baade, W. 1926, AN, 228, 359
Bartkowiak, A., & Jakimiec, M. 1989, AcA, 39, 85
Becker, A., 2015 HOTPANTS: High Order Transform of PSF ANd Template Subtraction, Astrophysics Source Code Library, ascl:1504.004
Bellm, E. C., Kulkarni, S. R., Graham, M. J., et al. 2019, PASP, 131, 018002
Bostroem, K. A., Dessart, L., Hillier, D. J., et al. 2023, ApJL, 953, L18
Bottinelli, L., Gouguenheim, L., Paturel, G., & de Vaucouleurs, G. 1984, A&AS, 56, 381
Bottinelli, L., Gouguenheim, L., Paturel, G., & Teerikorpi, P. 1986, A&A, 156, 157
Breeveld, A. A., Landsman, W., Holland, S. T., et al. 2011, in AIP Conf. Ser. 1358, Gamma Ray Bursts 2010, ed. J. E. McEnery, J. L. Racusin, & N. Gehrels (San Francisco, CA: ASP), 373
Brown, P. J., Breeveld, A. A., Holland, S., Kuin, P., & Pritchard, T. 2014, Ap&SS, 354, 89
Brown, P. J., Dessart, L., Holland, S. T., et al. 2007, ApJ, 659, 1488
Brown, P. J., Holland, S. T., Immler, S., et al. 2009, AJ, 137, 4517
Brown, T. M., Baliber, N., Bianco, F. B., et al. 2013, PASP, 125, 1031
Brown, T. M., Burleson, B., De Vera, J., et al. 2011, AAS Meeting Abstracts, 218, 132.02
Bruch, R. J., Gal-Yam, A., Schulze, S., et al. 2021, ApJ, 912, 46
Cardelli, J. A., Clayton, G. C., & Mathis, J. S. 1989, ApJ, 345, 245
Chugai, N., & Utrobin, V. 2024, AstL, 49, 639
Chugai, N. N., Chevalier, R. A., & Utrobin, V. P. 2007, ApJ, 662, 1136
Chugai, N. N., & Utrobin, V. P. 2000, A&A, 354, 557
Ciroi, S., Pignata, G., Benetti, S., et al. 2021, TNSCR, 2021-864
Clocchiatti, A., & Wheeler, J. C. 1997, ApJ, 491, 375
Czerny, B., Beaton, R., Bejger, M., et al. 2018, SSRv, 214, 32
Dastidar, R., Misra, K., Valenti, S., et al. 2019, MNRAS, 490, 1605
de Jaeger, T., Anderson, J. P., Galbany, L., et al. 2018, MNRAS, 476, 4592
de Jaeger, T., Zheng, W., Stahl, B. E., et al. 2019, MNRAS, 490, 2799
De Maesschalck, R., Jouan-Rimbaud, D., & Massart, D. 2000, Chemom. Intell. Lab. Syst., 50, 1
de Mello, D., Benetti, S., & Massone, G. 1997, IAU Circ., 6537, 1
de Vaucouleurs, G., Peters, W. L., Bottinelli, L., Gouguenheim, L., & Paturel, G. 1981, ApJ, 248, 408
Dessart, L., Blondin, S., Brown, P. J., et al. 2008, ApJ, 675, 644
Dessart, L., & Hillier, D. J. 2005, A&A, 439, 671
Dessart, L., & Hillier, D. J. 2020, A&A, 642, A33
Dessart, L., Hillier, D. J., & Audit, E. 2017, A&A, 605, A83
Dessart, L., Hillier, D. J., Waldman, R., & Livne, E. 2013, MNRAS, 433, 1745
Dong, Y., Valenti, S., Bostroem, K. A., et al. 2021, ApJ, 906, 56
Dopita, M. A., Kewley, L. J., Sutherland, R. S., & Nicholls, D. C. 2016, Ap&SS, 361, 61
Elmegreen, D. M., Chromey, F. R., McGrath, E. J., & Ostenson, J. M. 2002, AJ, 123, 1381
Elmhamdi, A. 2011, AcA, 61, 179
Fabricant, D., Fata, R., Epps, H., et al. 2019, PASP, 131, 075004
Fang, Q., & Maeda, K. 2018, ApJ, 864, 47
Fang, Q., Maeda, K., Kuncarayakti, H., Sun, F., & Gal-Yam, A. 2019, NatAs, 3, 434
Fang, Q., Maeda, K., Kuncarayakti, H., et al. 2022, ApJ, 928, 151
Faran, T., Poznanski, D., Filippenko, A. V., et al. 2014, MNRAS, 442, 844
Foreman-Mackey, D. 2016, JOSS, 1, 24
Foreman-Mackey, D., Hogg, D. W., Lang, D., & Goodman, J. 2013, PASP, 125, 306
Fuller, J. 2017, MNRAS, 470, 1642
Galbany, L., Anderson, J. P., Rosales-Ortega, F. F., et al. 2016, MNRAS, 455, 4087
Galbany, L., Anderson, J. P., Sánchez, S. F., et al. 2018, ApJ, 855, 107
Gall, E. E. E., Polshaw, J., Kotak, R., et al. 2015, A&A, 582, A3
Gal-Yam, A., Arcavi, I., Ofek, E. O., et al. 2014, Natur, 509, 471
Gal-Yam, A., Kasliwal, M. M., Arcavi, I., et al. 2011, ApJ, 736, 159
Garnavich, P. M., & Ann, H. B. 1994, AJ, 108, 1002
Gehrels, N., Chincarini, G., Giommi, P., et al. 2004, ApJ, 611, 1005
Gilkis, A., & Arcavi, I. 2022, MNRAS, 511, 691
Giraud, E. 1985, A&A, 153, 125
Goldberg, J. A., Jiang, Y.-F., & Bildsten, L. 2022, ApJ, 933, 164
González-Torà, G., Wittkowski, M., Davies, B., Plez, B., & Kravchenko, K. 2022, A&A, 669, A76
Graham, M. J., Kulkarni, S. R., Bellm, E. C., et al. 2019, PASP, 131, 078001
Gutiérrez, C. P., Anderson, J. P., Hamuy, M., et al. 2014, ApJL, 786, L15
Gutiérrez, C. P., Anderson, J. P., Hamuy, M., et al. 2017, ApJ, 850, 89
Hägele, G. F., Díaz, Á., Cardaci, M. V., Terlevich, E., & Terlevich, R. 2010, MNRAS, 402, 1005
Hamuy, M. 2003, ApJ, 582, 905
Hamuy, M., Pinto, P. A., Maza, J., et al. 2001, ApJ, 558, 615
Hamuy, M. A. 2001, PhD thesis, Univ. of Arizona
Harris, C. R., Millman, K. J., van der Walt, S. J., et al. 2020, Natur, 585, 357
Hillier, D. J., & Dessart, L. 2019, A&A, 631, A8
Hiramatsu, D., Howell, D. A., Moriya, T. J., et al. 2021a, ApJ, 913, 55
Hiramatsu, D., Howell, D. A., Van Dyk, S. D., et al. 2021b, NatAs, 5, 903

Hosseinzadeh, G., Farah, J., Shrestha, M., et al. 2023, ApJL, 953, L16
Hosseinzadeh, G., & Gomez, S. 2020, Light Curve Fitting, v0.2.0, Zenodo, doi:10.5281/zenodo.4312178
Hosseinzadeh, G., Kilpatrick, C. D., Dong, Y., et al. 2022, ApJ, 935, 31
Hosseinzadeh, G., Valenti, S., McCully, C., et al. 2018, ApJ, 861, 63
Humphreys, R. M., & Jones, T. J. 2022, AJ, 163, 103
Hunter, J. D. 2007, CSE, 9, 90
Jerkstrand, A. 2011, PhD thesis, Stockholm Univ.
Jerkstrand, A., Fransson, C., Maguire, K., et al. 2012, A&A, 546, A28
Jones, M. I., Hamuy, M., Lira, P., et al. 2009, ApJ, 696, 1176
Kansky, J., Chilingarian, I., Fabricant, D., et al. 2019, PASP, 131, 075005
Kasen, D., & Woosley, S. E. 2009, ApJ, 703, 2205
Kervella, P., Lagadec, E., Montargès, M., et al. 2016, A&A, 585, A28
Khazov, D., Yaron, O., Gal-Yam, A., et al. 2016, ApJ, 818, 3
Kirshner, R. P., & Kwan, J. 1974, ApJ, 193, 27
Kuncarayakti, H., Maeda, K., Bersten, M. C., et al. 2015, A&A, 579, A95
Kuriyama, N., & Shigeyama, T. 2020, A&A, 635, A127
Leonard, D. C., Filippenko, A. V., Barth, A. J., & Matheson, T. 2000, ApJ, 536, 239
Leonard, D. C., Kanbur, S. M., Ngeow, C. C., & Tanvir, N. R. 2003, ApJ, 594, 247
Levesque, E. M., Massey, P., Olsen, K. A. G., et al. 2005, ApJ, 628, 973
Marino, R. A., Rosales-Ortega, F. F., Sánchez, S. F., et al. 2013, A&A, 559, A114
Martinez, L., & Bersten, M. C. 2019, A&A, 629, A124
Masnan, M. J., Mahat, N. I., Shakaff, A. Y. M., et al. 2015, in AIP Conf. Ser. 1660 (Melville, NY: AIP), 050075
Matheson, T., Filippenko, A. V., Barth, A. J., et al. 2000, AJ, 120, 1487
Maund, J. R., Smartt, S. J., & Danziger, I. J. 2005, MNRAS, 364, L33
Mcley, L., & Soker, N. 2014, MNRAS, 445, 2492
Meza, N., Prieto, J. L., Clocchiatti, A., et al. 2019, A&A, 629, A57
Miralles-Caballero, D., Díaz, A. I., Rosales-Ortega, F. F., Pérez-Montero, E., & Sánchez, S. F. 2014, MNRAS, 440, 2265
Morag, J., Sapir, N., & Waxman, E. 2023, MNRAS, 522, 2764
Moriya, T. J., Pruzhinskaya, M. V., Ergon, M., & Blinnikov, S. I. 2016, MNRAS, 455, 423
Morozova, V., Piro, A. L., Renzo, M., et al. 2015, ApJ, 814, 63
Morozova, V., Piro, A. L., & Valenti, S. 2017, ApJ, 838, 28
Morozova, V., Piro, A. L., & Valenti, S. 2018, ApJ, 858, 15
Müller-Bravo, T. E., Gutiérrez, C. P., Sullivan, M., et al. 2020, MNRAS, 497, 361
Murai, Y., Tanaka, M., Kawabata, M., et al. 2024, MNRAS, 528, 4209
Narita, N., Fukui, A., Yamamuro, T., et al. 2020, Proc. SPIE, 11447, 114475K
Niemela, V. S., Ruiz, M. T., & Phillips, M. M. 1985, ApJ, 289, 52
Nieuwenhuijzen, H., & de Jager, C. 1990, A&A, 231, 134
Pastorello, A., Sauer, D., Taubenberger, S., et al. 2006, MNRAS, 370, 1752
Pastorello, A., Valenti, S., Zampieri, L., et al. 2009, MNRAS, 394, 2266
Pastorello, A., Zampieri, L., Turatto, M., et al. 2004, MNRAS, 347, 74
Pastoriza, M. G., Dottori, H. A., Terlevich, E., Terlevich, R., & Diaz, A. I. 1993, MNRAS, 260, 177
Pearson, J., Hosseinzadeh, G., Sand, D. J., et al. 2023, ApJ, 945, 107
Perley, D. 2021, TNSCR, 2021-8
Pessi, P. J., Folatelli, G., Anderson, J. P., et al. 2019, MNRAS, 488, 4239
Phillips, M. M., Simon, J. D., Morrell, N., et al. 2013, ApJ, 779, 38
Rodríguez, Ó., Pignata, G., Anderson, J. P., et al. 2020, MNRAS, 494, 5882
Polshaw, J., Kotak, R., Dessart, L., et al. 2016, A&A, 588, A1
Popov, D. V. 1993, ApJ, 414, 712
Poznanski, D., Prochaska, J. X., & Bloom, J. S. 2012, MNRAS, 426, 1465
Prochaska, J., Hennawi, J., Westfall, K., et al. 2020, JOSS, 5, 2308
Quataert, E., & Shiode, J. 2012, MNRAS, 423, L92
Quimby, R. M., Wheeler, J. C., Höflich, P., et al. 2007, ApJ, 666, 1093
Rabinak, I., & Waxman, E. 2011, ApJ, 728, 63
Rosales-Ortega, F. F., Kennicutt, R. C., Sánchez, S. F., et al. 2010, MNRAS, 405, 735
Rubin, A., Gal-Yam, A., De Cia, A., et al. 2016, ApJ, 820, 33
Sánchez, S. F., García-Benito, R., Zibetti, S., et al. 2016, A&A, 594, A36
Sanders, N. E., Soderberg, A. M., Gezari, S., et al. 2015, ApJ, 799, 208
Sapir, N., & Waxman, E. 2017, ApJ, 838, 130
Schlafly, E. F., & Finkbeiner, D. P. 2011, ApJ, 737, 103
Science Software Branch at STScI, 2012 PyRAF: Python alternative for IRAF, Astrophysics Source Code Library, ascl:1207.011
Shivvers, I., Groh, J. H., Mauerhan, J. C., et al. 2015, ApJ, 806, 213
Shrestha, M., Pearson, J., Wyatt, S., et al. 2024, ApJ, 961, 247
Silverman, J. M., Pickett, S., Wheeler, J. C., et al. 2017, MNRAS, 467, 369
Smartt, S. J. 2009, ARA&A, 47, 63
Smartt, S. J. 2015, PASA, 32, e016
Smith, N., & Arnett, W. D. 2014, ApJ, 785, 82
Soker, N. 2021, ApJ, 906, 1
Soumagnac, M. T., Ganot, N., Irani, I., et al. 2020, ApJ, 902, 6
Spiro, S., Pastorello, A., Pumo, M. L., et al. 2014, MNRAS, 439, 2873
Sravan, N., Marchant, P., & Kalogera, V. 2019, ApJ, 885, 130
Subrayan, B. M., Milisavljevic, D., Moriya, T. J., et al. 2023, ApJ, 945, 46
Sukhbold, T., Ertl, T., Woosley, S. E., Brown, J. M., & Janka, H. T. 2016, ApJ, 821, 38
Takáts, K., Pignata, G., Pumo, M. L., et al. 2015, MNRAS, 450, 3137
Takáts, K., Pumo, M. L., Elias-Rosa, N., et al. 2014, MNRAS, 438, 368
Tartaglia, L., Sand, D. J., Groh, J. H., et al. 2021, ApJ, 907, 52
Tartaglia, L., Sand, D. J., Valenti, S., et al. 2018, ApJ, 853, 62
Tsvetkov, D. Y., Volnova, A. A., Shulga, A. P., et al. 2006, A&A, 460, 769
Tully, R. B., & Fisher, J. R. 1988, Catalog of Nearby Galaxies (Cambridge: Cambridge Univ. Press)
Turatto, M., Mazzali, P. A., Young, T. R., et al. 1998, ApJL, 498, L129
Valenti, S., Howell, D. A., Stritzinger, M. D., et al. 2016, MNRAS, 459, 3939
Valenti, S., Sand, D., Pastorello, A., et al. 2014, MNRAS, 438, L101
Valenti, S., Sand, D. J., Wyatt, S., et al. 2021, TNSTR 2021-633
Van Dyk, S. D., Davidge, T. J., Elias-Rosa, N., et al. 2012, AJ, 143, 19
Vasylyev, S. S., Filippenko, A. V., Vogl, C., et al. 2022, ApJ, 934, 134
Virtanen, P., Gommers, R., Oliphant, T. E., et al. 2020, NatMe, 17, 261
Weaver, T. A., Zimmerman, G. B., & Woosley, S. E., 2017 KEPLER: General purpose 1D multizone hydrodynamics code, Astrophysics Source Code Library, ascl:1702.007
Wehner, E. H., Gallagher, J. S., Papaderos, P., Fritze-von Alvensleben, U., & Westfall, K. B. 2006, MNRAS, 371, 1047
Woosley, S. E., Eastman, R. G., Weaver, T. A., & Pinto, P. A. 1994, ApJ, 429, 300
Woosley, S. E., & Weaver, T. A. 1995, ApJS, 101, 181
Yaron, O., & Gal-Yam, A. 2012, PASP, 124, 668
Yaron, O., Perley, D. A., Gal-Yam, A., et al. 2017, NatPh, 13, 510
Young, T. R. 2004, ApJ, 617, 1233
Zampieri, L., Colpi, M., Shapiro, S. L., & Wasserman, I. 1998, ApJ, 505, 876
Zampieri, L., Pastorello, A., Turatto, M., et al. 2003, MNRAS, 338, 711
Zimmerman, E., Schulze, S., Johansson, J., et al. 2021, TNSAN, 2021-91